# Unsupervised Object-based Spectral Unmixing for Subpixel Mapping

Chengyuan Zhang [a], Qunming Wang [a, *], Peter M. Atkinson [b, c]

[a] College of Surveying and Geo-Informatics, Tongji University, 1239 Siping Road, Shanghai 200092, China

[b] Faculty of Science and Technology, Lancaster University, Lancaster LA1 4YR, UK

[c] Geography and Environment, University of Southampton, Highfield, Southampton SO17 1BJ, UK

*Corresponding author. E-mail: wqm11111@126.com.

*Abstract*: Subpixel mapping (SPM) addresses the widespread mixed pixel problem in remote sensing images by predicting the spatial distribution of land cover *within* mixed pixels. However, conventional pixel-based spectral unmixing, a key pre-processing step for SPM, neglects valuable spatial contextual information and struggles with spectral variability, ultimately undermining SPM accuracy. Additionally, while extensively utilized, supervised spectral unmixing is labor-intensive and user-unfriendly. To address these issues, this paper proposes a fully automatic, unsupervised object-based SPM (UO-SPM) model that exploits object-scale information to reduce spectral unmixing errors and subsequently enhance SPM. Given that mixed pixels are typically located at the edges of objects (i.e., the inner part of objects is characterized by pure pixels), segmentation and morphological erosion are employed to identify pure pixels within objects and mixed pixels at the edges. More accurate endmembers are extracted from the identified pure pixels for the secondary spectral unmixing of the remaining mixed pixels. Experimental results on 10 study sites demonstrate that the proposed unsupervised object (UO)-based analysis is an effective model for enhancing both spectral unmixing and SPM. Specifically, the spectral unmixing results of UO show an average increase of 3.65% and 1.09% in correlation coefficient ($R$) compared to Fuzzy-$C$ means (FCM) and linear spectral mixture model (LSMM)-derived coarse proportions, respectively. Moreover, the UO-derived results of four SPM methods (i.e., Hopfield neural network (HNN), Markov random field (MRF), pixel swapping (PSA) and radial basis function interpolation (RBF)) exhibit an average increase of 5.89% and 3.04% in overall accuracy (OA) across the four SPM methods and 10 study sites compared to the FCM and LSMM-based results, respectively. Moreover, the proportions of both mixed and pure pixels are more accurately predicted. The advantage of UO-SPM is more evident when the size of land cover objects is larger, benefiting from more accurate identification of objects.

*Keywords*: Mixed pixel, subpixel mapping (SPM), super resolution mapping, downscaling, spectral unmixing.

## 1. Introduction

Land cover mapping is crucial for environmental and land management, supporting various fields such as resource management, urban planning (Wang et al., 2018; Shi et al., 2022), disaster management (Shaw and Banba, 2017), carbon sequestration monitoring (Houghton et al., 2012; Holmberg et al., 2023) and climate modeling (Pielke Sr et al., 2011). Remote sensing is adopted widely for land cover mapping, due to the common advantages of raster image format, large synoptic coverage, internal precision of measurement and repeat visit capability (Auch et al., 2022; Brown et al., 2022). However, spaceborne remote sensing data, especially for large-scale and coarse spatial resolution scenes, commonly suffer from the mixed pixel problem where the spatial unit of the image (i.e., the pixel) may contain multiple land cover types on the ground. This makes the goal of conventional hard classification (i.e., one pixel one class) ill-defined, resulting in inaccurate boundaries and loss of distinct land cover types in thematic maps produced by this approach (Atkinson, 2009). Soft classification methods (e.g., spectral unmixing) can represent the multiple classes within pixels as proportions (Shi and Wang, 2014; Pfoch et al., 2023). Specifically, in spectral unmixing, classes are represented by endmembers (pure spectral signatures of different land cover types), and each mixed pixel in the scene is decomposed into proportions of these endmembers (Keshava, 2003; Plaza et al., 2011). However, the spatial position of each class *within* each pixel remains unknown in the coarse proportions, and it can be challenging to present such information in a single thematic map when the number of classes is large (Wang et al., 2014b). Subpixel mapping (SPM), also termed super-resolution mapping, is an effective solution to this issue. SPM can reveal the nature of class mixing (Fisher, 1997), encompassing both the land cover composition and the spatial arrangement of the classes within the mixed pixels.

Generally, the SPM approach divides pixels into smaller units (i.e., $s \times s$ subpixels, $s$ is the zoom factor) and assigns class labels to these units such as to map land cover at the finer spatial resolution. Due to the existence of multiple solutions to the spatial distribution within mixed pixels, SPM is inherently an ill-posed problem. To tackle this inverse problem, SPM relies on two core pillars: spatial prior and data fidelity. In essence, the spatial prior term specifies the rules for allocating land cover classes at the desired fine spatial resolution, thereby, reducing the space of possible solutions directly. Existing SPM methods focus predominantly on investigating various spatial prior terms, mainly through two streams. The first, spatial dependence or attraction, assumes that similar land cover classes tend to be located closer together. Conventional methods in this stream include the pixel swapping algorithm (PSA) (Atkinson, 2005), Hopfield neural network (HNN) (Tatem et al., 2002), Markov random field (MRF) (Kasetkasem et al., 2005) and radial basis function (RBF) (Wang et al., 2014a). The second stream aims to regularize the ill-posed problem by extending the spatial prior term through adding guidance on spatial details, involving panchromatic images (Nguyen et al., 2011), digital elevation models (Ling et al., 2008), seed labeled points (Chen et al., 2023), Google Earth images (He et al., 2022), temporally adjacent fine land cover maps (Li et al., 2021; Wang et al., 2022; Zhang et al., 2022), and coarse-to-fine image patches (Shang et al., 2020; Zhang et al., 2023). This type of spatial prior is effective and appealing when accessible. However, acquisition of the ancillary data is often laborious, and uncertainties may arise, such as registration error, scale difference and land cover changes over time.

The second pillar of SPM, the data fidelity term, is conventionally constructed through coarse proportion constraints, a universal strategy adopted by most SPM methods. Specifically, the underlying principle is that the number of subpixels for each land cover class within the coarse pixels should conform to predefined proportions. This coarse proportion information is generally extracted by applying spectral unmixing to the original coarse spatial resolution multi-spectral images, implying that spectral unmixing serves as a pre-processing step for SPM. However, as a widely acknowledged open issue, spectral unmixing-predicted proportions, for input to SPM, are not error-free (Dong et al., 2022). For example, the PSA and RBF methods, which adhere strictly to the coarse proportions, generate noise-like erroneously labeled subpixels when errors exist in the proportions. To handle this situation, certain SPM approaches adopt a more lenient interpretation of the coarse proportions constraint to obtain a more smoothed result. For example, MRF imports a spectral constraint term to balance data fidelity between the real spectral images and the proportion constraints. Additionally, the HNN model employs soft values (ranging from 0 to 1) instead of hard labels (certain to be 0 or 1) to represent class probabilities for each subpixel. These methods can partially mitigate minor noise-like erroneous subpixels in the SPM process. However, they fall short of dealing fully with proportion-dependent error in the SPM results. Moreover, the misclassified subpixels brought by errors in the coarse proportions have a negative effect on the spatial prior term of SPM.

To circumvent the reliance on spectral unmixing results, He et al. (2021) proposed an end-to-end deep-learning-based framework for SPM that omits the intermediate spectral unmixing step, with more attention on a learning sub-scale spatial pattern prior. However, the outcomes show that land cover categories may not be retrieved without the coarse proportion constraints. In contrast, methods with proportion constraints can recover all the land cover classes of interest, but may inherit any proportional errors in the final fine land cover maps. Hence, it is imperative to provide reliable class proportions for more accurate SPM results.

To mitigate errors in the coarse proportions, Yin et al. (2023) introduced a fraction (i.e., proportion) error eliminating convolutional neural network (CNN) model. Using training data obtained by adding simulated Gaussian-distributed errors to error-free proportions obtained through degrading the target, the network enables learning about the proportional errors. To reduce shadow effects, Hao et al. (2023) optimized the proportions by incorporating water, vegetation and shadow index features. Wang et al. (2020) addressed the effect of the point spread function through a Gaussian convolution kernel, obtaining enhanced coarse proportions as input for SPM. However, traditional pixel-level interpretation of spectral signatures faces challenges when dealing with complex land cover structures (Borsoi et al., 2021). This challenge is exacerbated when there is significant spectral variability among land cover classes, originating from variation in material properties, environmental conditions, illumination angles and sensor characteristics (Wang et al., 2016; Wang et al., 2022). Hence, it becomes necessary to explore information not only on the spectrum of individual pixels, but also from the perspective of spatial contextual information.

In the hard classification domain, object-based image analysis can be effective for extracting spatial contextual information with reduced sensitivity to noise and variation (Hao et al., 2024), yet challenges persist in addressing the mixed pixel problem. Within the SPM domain, the literature on object-based SPM models is limited. For example, Ling et al. (2012) refined building mapping by extracting the main orientation of each building object as a spatial prior. Chen et al. (2017) shifted the conventional class allocation strategy from subpixel or class units to an object level for soft-then-hard SPM methods (Wang et al., 2014b). Nevertheless, object-scale information in these methods is employed for allocating subpixels with proportion constraints, retaining errors from spectral unmixing. Consequently, as a crucial pre-processing step of SPM, spectral unmixing necessitates object-oriented analysis to fully utilize neglected spatial contextual information within remote sensing images.

Early developments in spectral unmixing generally exploited spectral information alone. Given that remote sensing images contain both spatial and spectral information (Xu et al., 2022), incorporating spatial information into spectral unmixing has gained increasing attention in recent years (Shi and Wang, 2014; Hong et al., 2024). Existing methods for integrating spatial information into spectral unmixing focus primarily on two aspects. First, in the step of endmember selection, spatial information is used to find the purest or most representative endmembers (Plaza et al., 2002; Deng and Wu, 2013) or to share endmember combinations within spatially homogenous regions (Zare et al., 2013). Second, in the step of coarse proportion estimation, spatial information is considered by maximizing the spatial coherence among adjacent neighbors (Borsoi et al., 2020; Cao et al., 2022). Overall, the utilization of spatial information has shown great potential for enhancing spectral unmixing. However, these methods are fundamentally pixel-wise methods for unmixing the original images, meaning that object-scale information in the unmixing results is not fully leveraged. Furthermore, before the implementation of SPM, supervised spectral unmixing is typically conducted to obtain the input coarse proportions, which requires selection of endmembers. Unsupervised SPM models, which are more convenient and user-friendly, are rarely considered in existing methods.

This paper introduces an unsupervised and automatic object-based SPM (UO-SPM) model to enhance SPM for both mixed and pure pixels concurrently. The object-based analysis is applied following an unsupervised soft classification process to group coarse proportions into objects. Recognizing that mixed pixels are often located at the intersection areas of different land cover classes (edges of objects) in real geographical scenes, a morphological operation is implemented to discriminate pure pixels within objects and mixed pixels at the edges of objects. Subsequently, pure pixels are less likely to be misidentified, and more accurate pure spectral signatures are more likely to be utilized for the secondary spectral unmixing of the remaining mixed pixels. Ultimately, the proposed UO-SPM model, with its comprehensive analysis of object-scale, pixel-scale and subpixel-scale information, can increase the accuracy of spectral unmixing and ultimately SPM without requiring additional human input. The main contributions are three-fold. First, an object-based strategy is proposed for SPM. The UO-SPM model effectively detects mixed pixels through object-based analysis, specifically focusing on the edges of objects. These detected mixed pixels are further enhanced through a supervised secondary spectral unmixing process. Second, the proposed UO-SPM is an entirely automatic unsupervised SPM model, taking coarse spectral images as input to generate fine spatial resolution land cover maps without manual input. The proposed model is adaptable to various SPM algorithms utilizing coarse proportions as part of the data fidelity term and is validated on diverse conventional algorithms, including PSA, RBF, HNN and MRF. Third, the characterization of spatial dependence in SPM is shifted from the pixel level to the object level. With UO-SPM, pure pixel information within objects is further utilized as prior information when allocating land cover classes within mixed pixels.

The remainder of this paper is structured as follows. Section 2 outlines the flowchart of UO-SPM, followed by a comprehensive description of each stage, encompassing unsupervised soft classification, object-based identification of mixed and pure pixels, and spectral unmixing and SPM for the remaining mixed pixels.

Section 3 demonstrates the effectiveness of UO-SPM based on experimental results on three multi-spectral datasets. Section 4 discusses open issues related to UO-SPM and Section 5 concludes the paper.

## 2. Methods

The flowchart of the UO-SPM model is illustrated in Fig. 1 with three main stages. The detailed explanations of each stage are provided below.

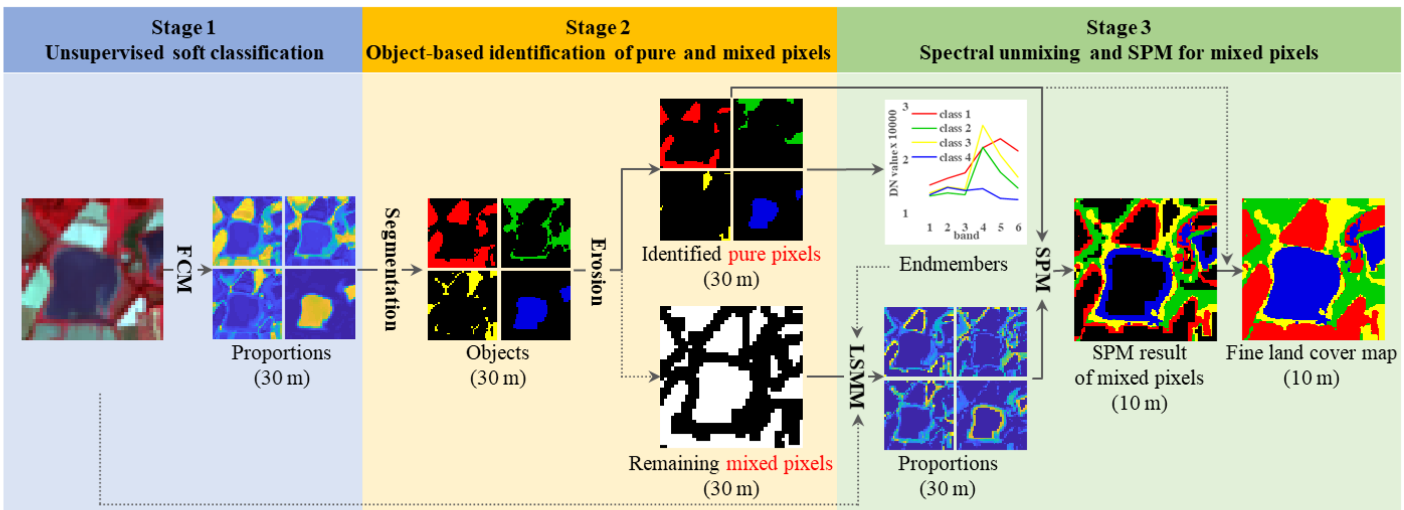


SPM: Subpixel mapping
FCM: Fuzzy C-Means algorithm (an unsupervised spectral unmixing method)
LSMM: Linear spectral mixture model (a supervised spectral unmixing method)

Fig. 1. Flowchart of the proposed unsupervised object-based subpixel mapping (UO-SPM).

### *2.1. Unsupervised soft classification*

In the conventional SPM workflow, when dealing with a coarse spatial resolution multi-spectral image, the initial step involves employing a spectral unmixing model to derive the coarse proportions. The LSMM, chosen for its simplicity and physical interpretability, is applied widely as a pre-processing step in existing SPM models (Olthof and Fraser, 2024). Then the coarse proportions are utilized directly in SPM, providing the data coherence term. However, the spectral unmixing technique faces uncertainties in addressing the spectral variation problem of land cover classes, irrespective of the chosen models, and errors inevitably impact the SPM process negatively. In the proposed UO-SPM model, an unsupervised Fuzzy-*C* means (FCM) technique is utilized to generate an initial soft classification result, forming the basis for subsequent object-based analysis.

As shown in Fig. 1, the unsupervised FCM method is applied directly on the coarse spatial resolution multi-spectral image. The FCM is essentially an unsupervised clustering algorithm with the objective of minimizing the dissimilarity between data points (i.e., pixels) and cluster centers of land cover classes. Instead of forcing to a specific cluster, FCM assigns membership degrees, which represent the probabilities of belonging to each cluster. Given *N* pixels in the coarse spatial resolution multi-spectral image $\mathbf{y}$, the objective function is defined as

$$\begin{aligned} &\min F = \sum_{n=1}^{N}\sum_{k=1}^{C}(\mu_k(n))^m \left\|\mathbf{y}_n - \mathbf{v}_k\right\|^2 \\ &s.t.\, \mu_k(n) \in [0,1], \sum_{k=1}^{C}\mu_k(n) = 1 \text{ and } \sum_{n=1}^{N}\mu_k(n) > 0 \end{aligned} \tag{1}$$

in which $C$ is the total number of clusters, *m* is a fuzziness index that determines the level of fuzziness, $\mathbf{v}_k$ is the center of cluster *k*, and $\mu_k(n)$ is the membership degree of pixel *n* to cluster *k* with the constraints.

The fuzzy membership values generated by FCM exhibit correlation with the actual proportions of land covers on the ground (Fisher and Pathirana, 1993). However, these values, while helpful in representing individual pixels, often neglect the contextual information within objects. This oversight can result in large errors in the spectral unmixing results. To address this limitation, a two-step object-oriented approach is adopted. Initially, segmentation and erosion operations are applied to the fuzzy map predicted by FCM, enhancing the delineation of object boundaries (introduced in Section 2.2). Subsequently, the mixed pixels within these objects, characterized with reduced errors, undergo supervised spectral unmixing for increased accuracy (introduced in Section 2.3).

### 2.2. Object-based identification of pure and mixed pixels

#### 2.2.1. Segmentation

Segmentation is not applied directly to the original multi-spectral images, but rather to the FCM results for two primary reasons. First, FCM offers a representation of the uncertainty in the data, making it valuable for addressing regions with overlapping diverse land cover classes. Second, over- and under-segmentation can occur easily when applied to the original data, while FCM provides greater flexibility in handling clusters of various shapes. In this paper, the Otsu algorithm (Otsu, 1979) is employed to find the optimal threshold automatically for segmenting the coarse proportions into background and foreground objects for each land cover class. The Otsu algorithm operates on histogram-based principles with the goal of maximizing inter-class variance between two classes and minimizing the intra-class variance simultaneously. This aligns with the concept of coarse proportions with errors for each land cover class. Given one cluster of the FCM result, the optimal threshold is found by testing intensity levels that can maximize the inter-class variance.

#### 2.2.2. Pixel identification by morphological erosion

Mixed pixels are generally located at the intersection of different land cover types, that is, the edge pixels of objects. Moreover, the Otsu algorithm may face challenges when the proportion of a certain class is small or when the background is complex (e.g. simultaneous presence of forest and grass classes). Therefore, morphological erosion is applied consecutively to exclude pixels located at the edge of objects, which are more likely to be mixed pixels. This approach effectively addresses the intra-spectral variability problem by identifying inner pixels of objects (more likely to be pure pixels) through the segmentation of the FCM results into objects, for each land cover class in the FCM results. Overall, this segmentation-then-erosion step is the key to coping with the problem of complex land cover structures with evitable spectral variation by fully utilizing the latent contextual object-based information in the coarse proportions.

### *2.3. Spectral unmixing and SPM for mixed pixels*

#### *2.3.1. Spectral unmixing for remaining mixed pixels*

The LSMM method is utilized, but plays distinct roles compared to FCM in the UO-SPM framework. Specifically, the FCM method serves as the foundation of the subsequent segmentation and erosion steps, while the purpose of utilizing LSMM is to further increase the unmixing accuracy of the identified remaining mixed pixels. In LSMM, the spectral response of a mixed pixel is viewed as a linear weighted sum of its component land cover spectra in that pixel, expressed by

$$\begin{gathered} \mathbf{y}_n = \sum_{k=1}^{C} \mathbf{E}_k f_k + \mathbf{e} \\ s.t. f_k \geq 0 \ (k = 1, \ldots, C) \text{ and } \sum_{k=1}^{C} f_k = 1 \end{gathered} \tag{2}$$

in which $\mathbf{y}_n$ is the vector for spectral responses in $B$ wavebands of a pixel *n*, $f_k$ is the proportional coverage of class *k* in the observed pixel and $\mathbf{e}$ is a residual error term. The columns of $\mathbf{E}_k$ represent pure spectra of the *k* land cover class in the absence of noise, commonly derived from pre-defined pure pixels. Once **E** is defined, the mixture model can estimate the class composition $f_k$ of a pixel from its spectral response $\mathbf{y}_n$ subject to the constraints.

The endmember matrix **E** is commonly derived from manual selection of pure pixels. However, this approach is laborious, making it unsuitable for mapping diverse regions in real-world scenes. In the UO-SPM, the endmembers are approximated by calculating for the filtered inner pixels of objects (more likely to be pure pixels) in the segmentation-then-erosion process. That is, **E** is acquired readily from the identified pure pixels for each land cover class. Additionally, the identified pure pixels belonging to different land cover classes inherently exhibit inter-class spectral variability. Therefore, the extraction of pure spectra is abundantly accessible and more comprehensive for diverse regions compared to labor-intensive manual selection.

#### *2.3.2. SPM for the remaining mixed pixels*

In general, SPM models use the spatial attraction and data fidelity terms to predict the fine spatial resolution land cover map $\hat{\mathbf{X}}$, which can be formulated as

$$\hat{\mathbf{X}} = \arg\max(A(\mathbf{X})) + \arg\min(D(\mathbf{X},\mathbf{Y},\mathbf{H})) \quad (3)$$

where $\mathbf{Y} = [y_1^1, y_2^1 ... y_N^1, y_1^2, y_2^2 ... y_N^2 ... y_N^C]$ denotes the coarse spatial resolution coarse proportion image with $N$ pixels for $C$ land cover classes, $\mathbf{X} = [x_1, x_2, ..., x_{s\times N}]$ is the resultant fine land cover map, $A(\mathbf{X})$ is the summary of spatial attraction between each subpixel in **X** and its spatial neighbors, **H** represents the degradation process between **X** and **Y**, and $D(\mathbf{X},\mathbf{Y},\mathbf{H}) = \| \mathbf{Y} - \mathbf{HX} \|_2^2$, which represents the data coherence between the predicted fine land cover map and the coarse proportion.

In the proposed UO-SPM model, benefitting from the object-based pixel identification step, the two terms can be expressed based on the identified pure objects and the remaining mixed pixels as:

$$\hat{\mathbf{X}} = A(\mathbf{X}_{object}) + D(\mathbf{X}_{object}) + \arg\max(A(\mathbf{X}_{pixel}) + A(\mathbf{X}_{pixel-to-obejct})) + \arg\min(D(\mathbf{X}_{pixel},\mathbf{Y},\mathbf{H})) \quad (4)$$

in which $\mathbf{X}_{object}$ and $\mathbf{X}_{pixel}$ represent the detected pure pixels in objects and the remaining mixed pixels, respectively, while $A(\bullet)$ and $D(\bullet)$ are the spatial attraction term and data fidelity term, respectively. Ideally, the spatial attraction term of pure pixels in objects $A(\mathbf{X}_{object})$ is maximized, yielding a zero value for $D(\mathbf{X}_{object})$ if the detection of mixed and pure pixels is correct. Through the object-based analysis, pure pixels inside objects are included after the erosion step, and the remaining mixed pixels are further decomposed by supervised spectral unmixing. Thereby, prediction for the remaining pixels can utilize the object-scale information (i.e., the settled inner pure pixels of objects) as a spatial prior to reduce the uncertainties in SPM, as represented by the spatial dependence term $A(\mathbf{X}_{pixel-to-obejct})$ in Eq. (4).

The UO-SPM is proposed to reduce errors in spectral unmixing through unsupervised object-based analysis, and ultimately increase the accuracy of SPM. Thus, UO-SPM is a universal model instead of a specific SPM algorithm. After detecting pure pixels and unmixing mixed pixels using the UO-based strategy, the final SPM of the remaining mixed pixels can be conducted by any existing SPM methods that use spectral unmixing as a pre-processing step.

## 3. Experiments

### *3.1. Study area and datasets*

To evaluate the effectiveness of the proposed UO-SPM approach, experiments were conducted on 10 study sites (Fig. 2 and Table 1). The locations of these sites on the world map and their corresponding input coarse images are shown in Fig. 2. For Site 1, the 80 m coarse multi-spectral image used as input for SPM was derived by degrading a 10 m reference Sentinel-2 multi-spectral image acquired on July 3, 2019 with a scale factor of eight. For Sites 2-10, the 30 m multi-spectral Landsat images used as inputs for SPM were acquired from the United States Geological Survey (USGS) (https://earthexplorer.usgs.gov/). The center coordinates, acquisition dates, sizes of the input coarse images (i.e., 30 m Landsat) and 10 m Sentinel-2 reference images are listed in Table 1. For quantitative evaluation, the fine spatial resolution land cover maps (Lines 2 and 4 of Fig. 3) for the study areas were obtained using a support vector machine (SVM) applied to the temporally closest 10 m multi-spectral Sentinel-2 images (Lines 1 and 3 of Fig. 3) acquired from the Copernicus European Space Agency hub (https://dataspace.copernicus.eu/). The zoom factor of SPM was eight for Site 1 and three for Sites 2-10.

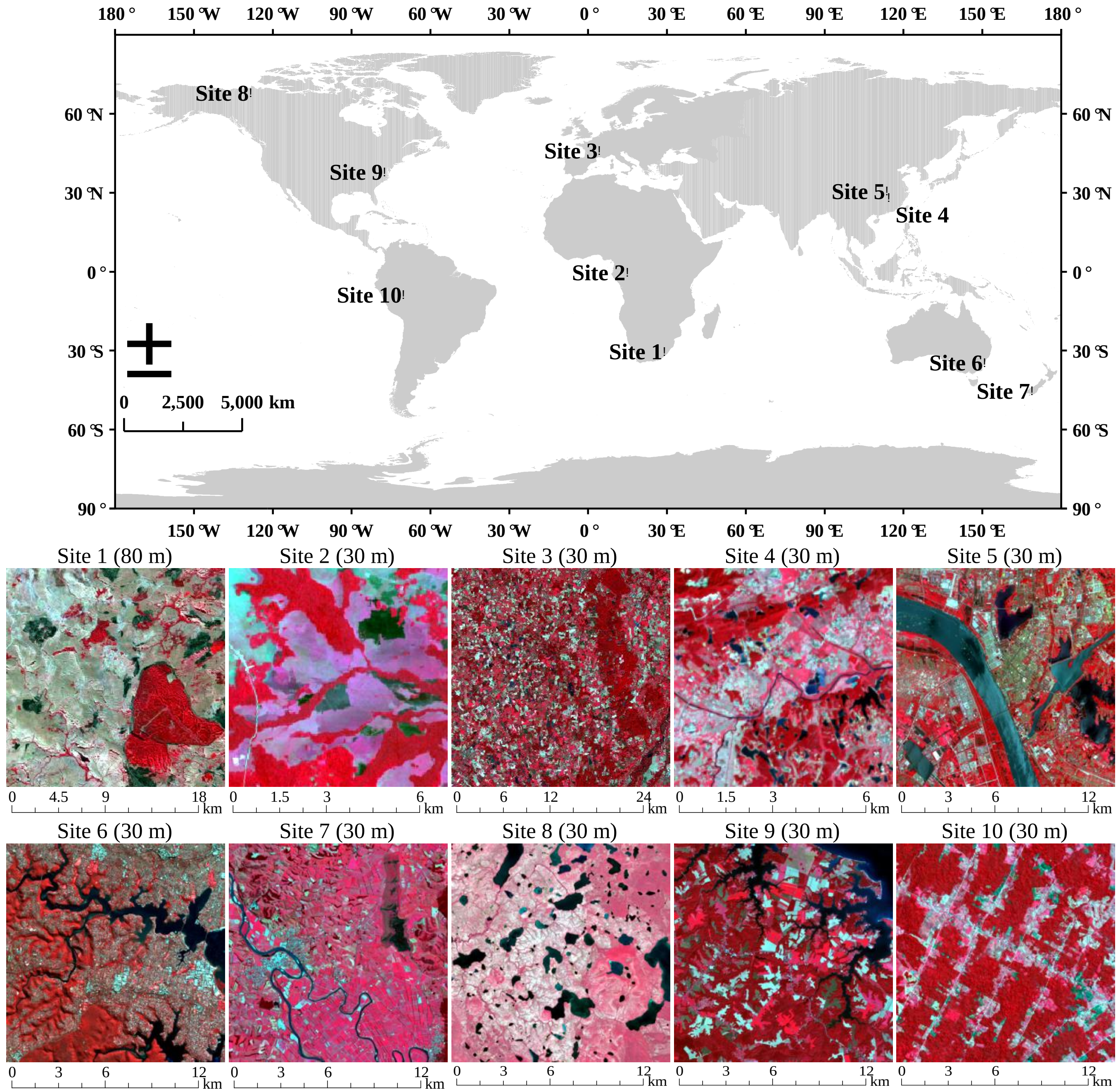


Fig. 2. The locations of the 10 study sites on the world map and their corresponding input coarse spatial resolution images. The false color coarse images are composited using Near-Infrared (NIR), Red and Green bands as RGB.

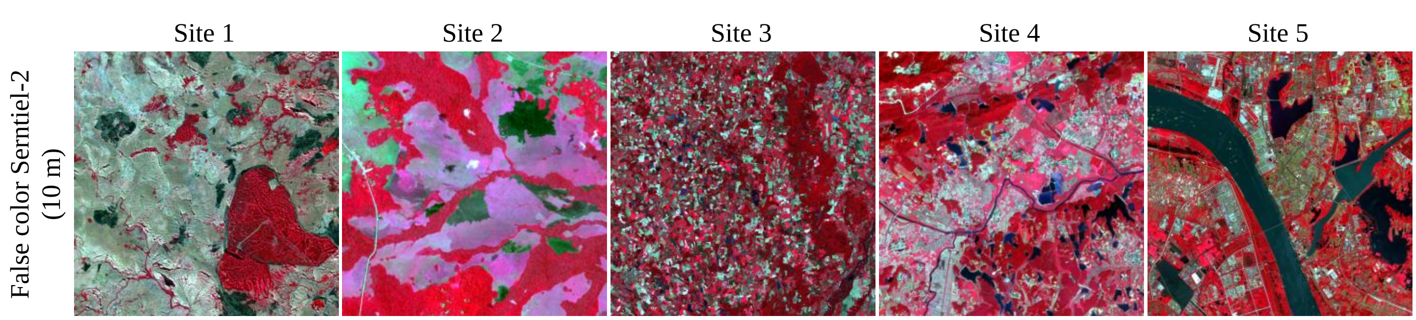

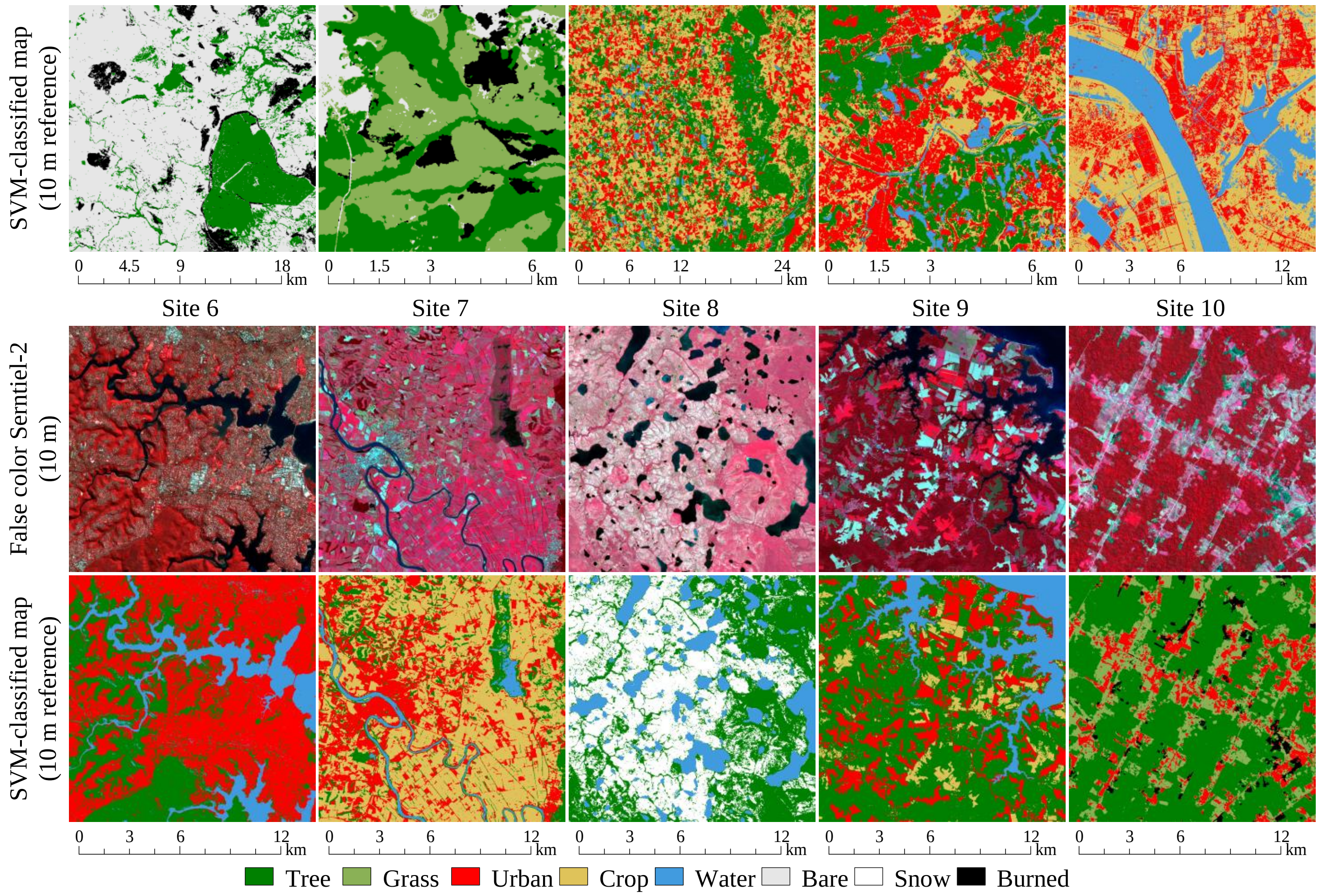


Fig. 3. The 10 m false-color Sentinel-2 images and the corresponding land cover maps derived with a support vector machine (SVM) used for accuracy assessment.

Table 1 Detailed information of the 10 study sites

| Site | Center coordinates | | Source of input coarse multi-spectral images | Acquisition date of Coarse images (Month/Day/Year) | Size of coarse images | Acquisition date of Sentinel-2 images (Month/Day/Year) | Size of fine reference land cover maps | Zoom factor of SPM |
|---|---|---|---|---|---|---|---|---|
| 1 | 30°17’ S | 29°50’ E | Degraded Sentinel-2 | 07/03/2019 | 225×225 | 07/03/2019 | 1800×1800 | 8 |
| 2 | 0°17’ S | 15°46’ E | Landsat 8 | 09/07/2022 | 200×200 | 09/07/2022 | 600×600 | 3 |
| 3 | 46°03’ N | 5°10’ E | Landsat 9 | 10/06/2023 | 800×800 | 10/06/2023 | 2400×2400 | 3 |
| 4 | 28°08’ N | 115°16’ E | Landsat 9 | 10/16/2023 | 200×200 | 10/16/2023 | 600×600 | 3 |
| 5 | 30°28’ N | 114°33’ W | Landsat 8 | 06/08/2023 | 400×400 | 06/09/2023 | 1200×1200 | 3 |
| 6 | 34°01’ S | 151°4’ E | Landsat 8 | 07/12/2023 | 400×400 | 07/13/2023 | 1200×1200 | 3 |
| 7 | 45°14’ S | 169°45’ E | Landsat 9 | 01/07/2023 | 400×400 | 01/08/2023 | 1200×1200 | 3 |
| 8 | 67°58’ N | 127°28’ W | Landsat 9 | 06/25/2023 | 400×400 | 06/25/2023 | 1200×1200 | 3 |
| 9 | 37°58’ N | 76°31’ W | Landsat 9 | 10/02/2023 | 400×400 | 10/02/2023 | 1200×1200 | 3 |
| 10 | 8°48’ S | 69°22’ W | Landsat 8 | 08/26/2023 | 400×400 | 08/27/2023 | 1200×1200 | 3 |

### *3.2. Benchmark methods and evaluation indices*

As previously mentioned, the UO-SPM model can be integrated with any SPM method that uses spectral unmixing as a pre-processing step. The UO-SPM model addresses errors in spectral unmixing through unsupervised object-based analysis. To validate the benefits of the unsupervised object-based (UO) analysis, we examined the performance of UO-SPM using four conventional SPM algorithms, including HNN, MRF, PSA and RBF. These methods exhibit distinct characteristics in terms of spatial and data fidelity terms. At the object-scale, subpixels within the inner part of objects (i.e., identified pure pixels) are assigned to their corresponding class across all SPM methods. Regarding the pixel-scale information (i.e., coarse proportions of the remaining mixed pixels), the HNN and MRF methods do not adhere strictly to the coarse proportions, while PSA and RBF comply strictly with the coarse proportions. Moreover, the object scale information (i.e., subpixels that are assigned to one class already) aids in predicting the remaining subpixels through the spatial attraction term. This term is defined between subpixels and subpixels for methods including MRF, HNN and PSA, while for RBF it operates between subpixels and pixels. More details can be found for PSA in Atkinson (2005), HNN in Nguyen et al. (2006), MRF in Tolpekin and Hamm (2008) and RBF in Wang et al. (2014a). Moreover, the morphological filtering and fraction refilling (MFFR) algorithm (Ling et al., 2014) was used as a benchmark, involving interpolation, morphological operations (e.g., erosion or opening) and final optimization of the SPM result.

For comparison, the original unsupervised FCM and supervised LSMM were also implemented for the four SPM algorithms. In summary, 16 methods were examined, namely, UO-HNN, UO-MRF, UO-PSA, UO-RBF, FCM-HNN, FCM-MRF, FCM-PSA, FCM-RBF, FCM-MFFR-erode, FCM-MFFR-open, LSMM-HNN, LSMM-MRF, LSMM-PSA, LSMM-RBF, FCM-MFFR-erode and LSMM-MFFR-open. Note that the MFFR method is a type of object-based method. Therefore, it was not integrated into the UO-based model and compared with the UO-SPM methods directly. During the experiments, the parameters for all methods were set empirically or based on suggestions from the existing literature. Specifically, the window size was set to $3\times3$ subpixels for MRF and HNN, $5\times5$ subpixels for PSA and MFFR, and $3\times3$ pixels for RBF. The morphological structure size was set to 3 for the UO-based methods (i.e., UO-HNN, UO-MRF, UO-PSA and UO-RBF) and the MFFR-based methods (i.e., FCM-MFFR-erode, FCM-MFFR-open, LSMM-MFFR-erode and LSMM-MFFR-open).

### *3.3. Spectral unmixing results*

The proposed UO-SPM model addresses errors caused by the spectral unmixing process. Consequently, it is crucial to assess the coarse proportions with and without considering the object-based analysis. To this end, the UO-based spectral unmixing results were compared to those obtained using the FCM and LSMM methods.

For visual comparison, the spectral unmixing results and error images for sites 1, 4 and 9, presented in Figs. 4-6, respectively, reveal noteworthy distinctions among the three methods. The error images were generated by comparing the spectral unmixing results to the ideal proportions, with the latter derived by degrading the SVM-based fine spatial resolution land cover map with the corresponding zoom factor for each site. The second line in Figs. 4-6 depicts the results produced by the FCM-based spectral unmixing method. Clustering pixels with spectral similarity tends to generate ambiguous and over-smoothed proportion images at the boundaries of land cover classes. The third line displays the results obtained through LSMM, revealing numerous noise pixels in the backgrounds of the land cover classes, misidentified as mixed pixels. In contrast, the UO-derived unmixing results, depicted in the fourth line, exhibit proportions that are closer to the ideal proportions, particularly for the inner regions of objects. The error images indicate that the FCM and LSMM results generally exhibit larger errors, with more pixels displaying both overestimated and underestimated proportion errors. The error images in Figs. 4-6 reveal a larger number of error pixels with deeper colors in the FCM and LSMM results compared to those of the UO results. In summary, visual comparison between the coarse proportions and error images emphasizes that the proportion error is the smallest for the object-based analysis in the UO-SPM framework, outperforming the other two spectral unmixing methods.

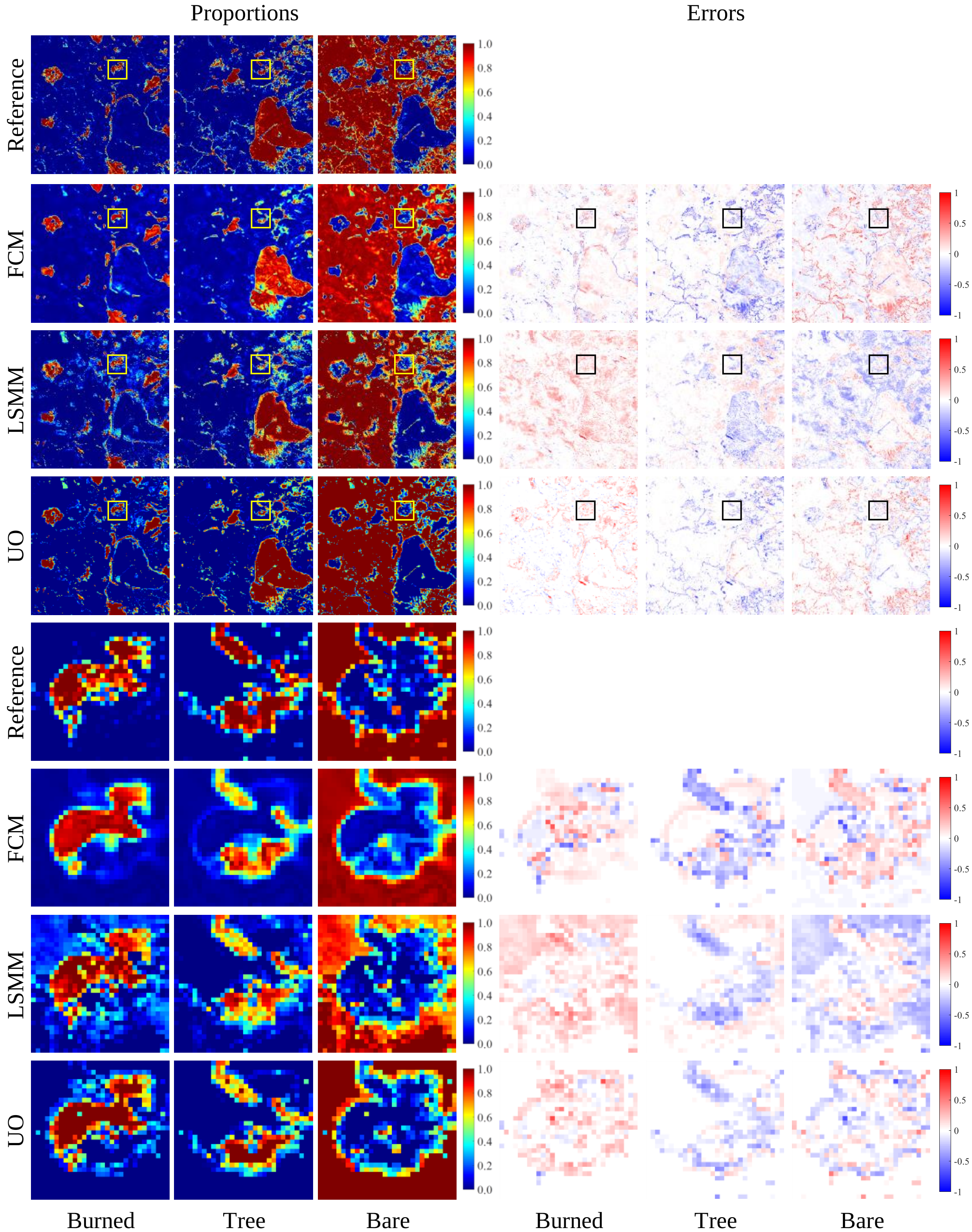


Fig. 4. Spectral unmixing results, corresponding proportion error maps (compared to the ideal coarse proportions derived by degrading the reference land cover map with a zoom factor of three) and zoom-in scenes for site 1 (with a zoomed subarea in the last four lines).

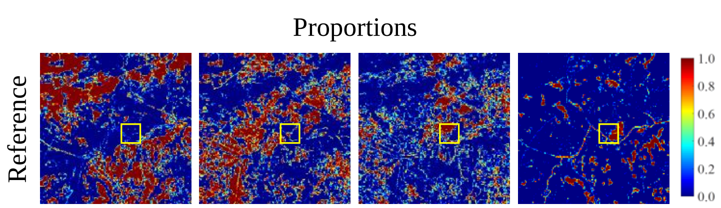

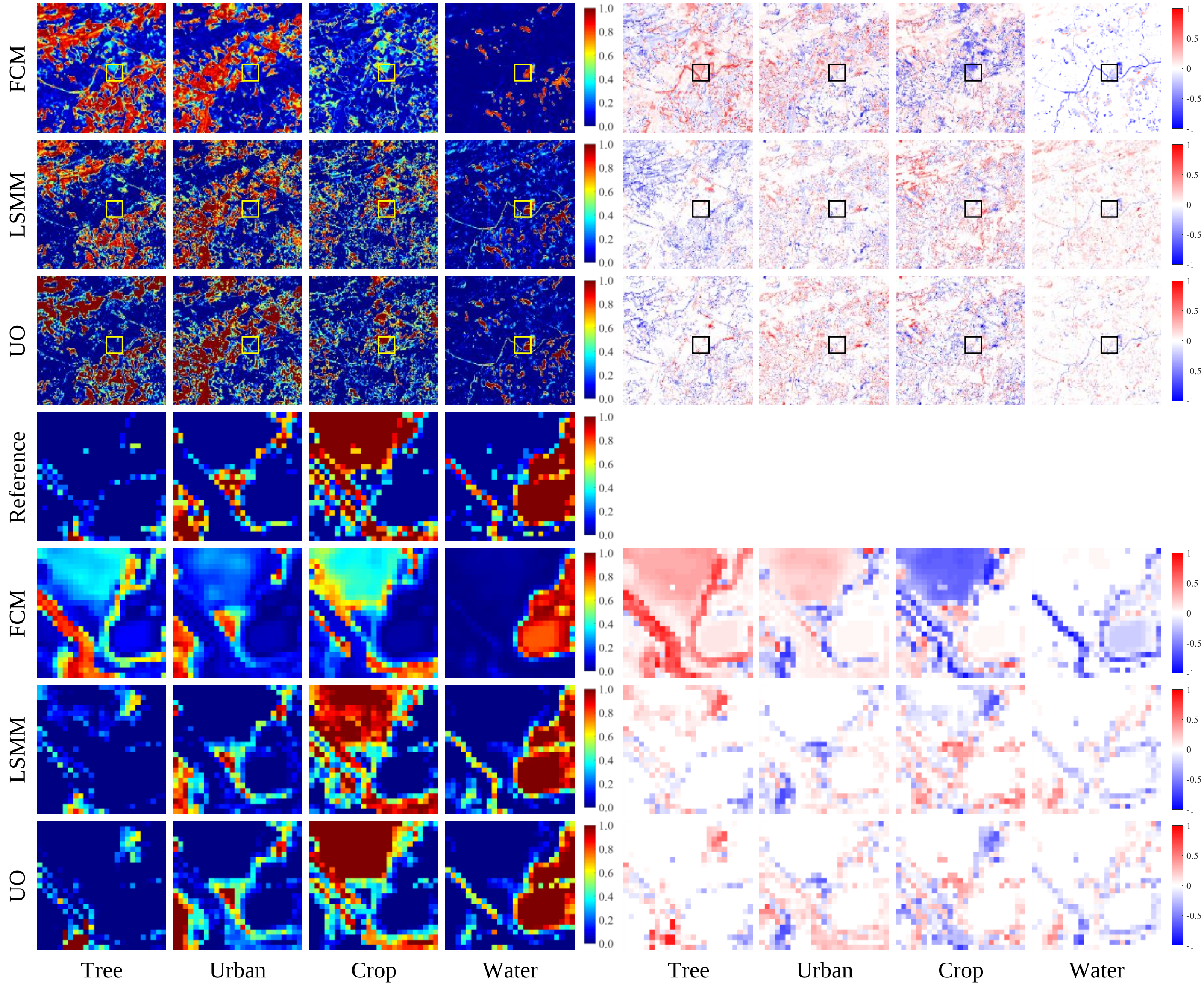


Fig. 5. Spectral unmixing results, corresponding proportion error maps (compared to the ideal coarse proportions derived by degrading the reference land cover map with a zoom factor of three) and zoom-in scenes for Site 4 (with a zoomed subarea in the last four lines).

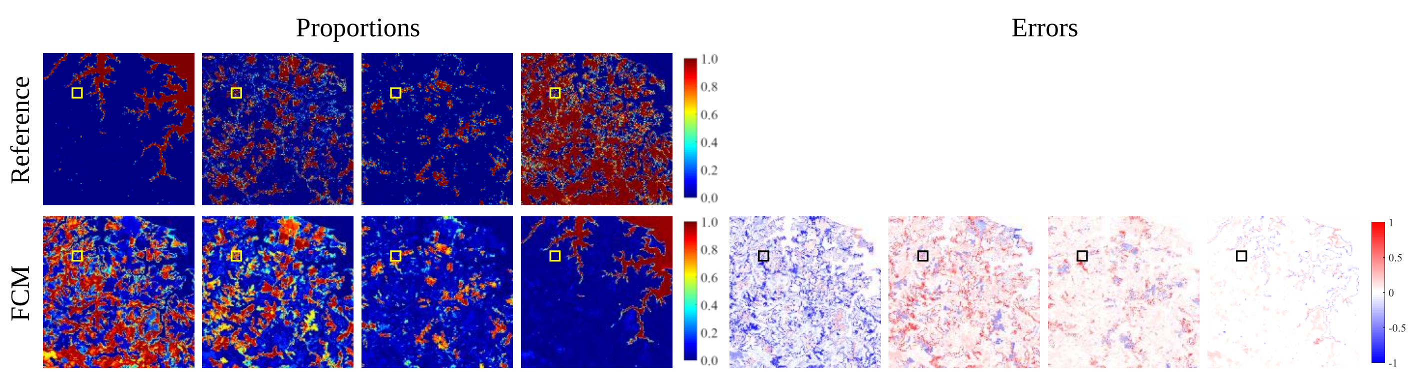

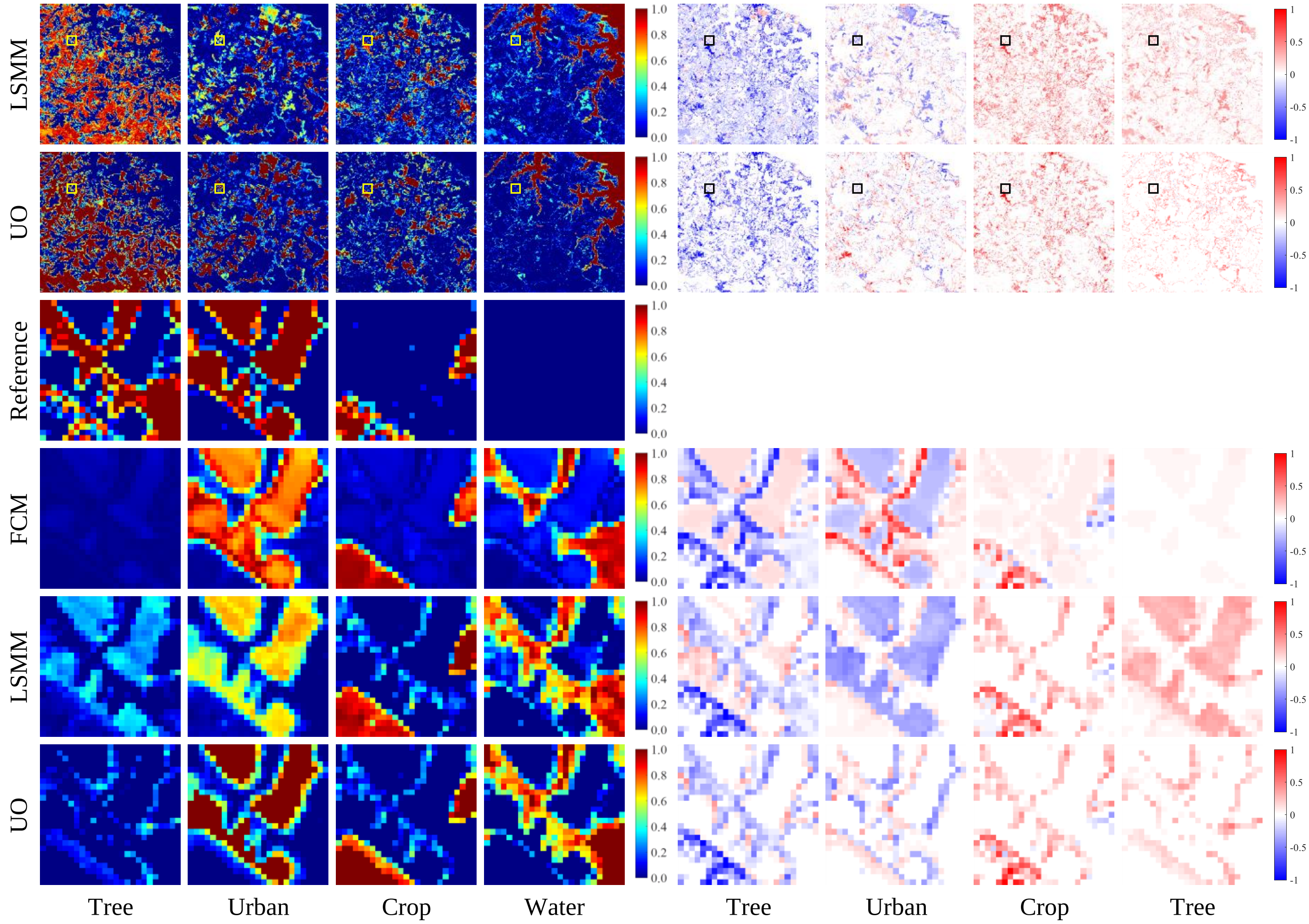


Fig. 6. Spectral unmixing results, corresponding proportion error maps (compared to the ideal coarse proportions derived by degrading the reference land cover map with a zoom factor of three) and zoom-in scenes for Site 9 (with a zoomed subarea in the last four lines).

Quantitative evaluation of the spectral unmixing results for the 10 sites was conducted based on the correlation coefficient ($R$), root-mean-square-error (RMSE) and mean-absolute-error (MAE) between the spectral unmixing results and the ideal coarse proportions (obtained by degrading the reference land cover map with the zoom factor of each site). For clearer comparison, the differences in $R$, RMSE and MAE between the spectral unmixing results of the UO and FCM (denoted as 'UO than FCM') and those of the UO and LSMM (denoted as 'UO than LSMM') are listed in Table 2, as highlighted in bold.

In alignment with the visual evaluation presented in Figs. 4-6, the results for the LSMM surpass those of FCM, with larger $R$ and smaller RMSE and MAE values. This suggests that the resulting coarse proportions generated by unsupervised FCM are less accurate than LSMM. Moreover, the UO method produces the most accurate coarse proportions across the 10 sites, as indicated by the largest *R*, and smallest RMSE and MAE values overall. More precisely, the *R* value of the UO method surpasses that of the FCM and LSMM results by an average of 3.65% and 1.10%, respectively. The MAE and RMSE values of UO are decreased by an average of 15.22% (an absolute decrease of 0.0302) and 37.33% (an absolute decrease of 0.0453), respectively, compared to those of the FCM method. Compared to the LSMM method, the MAE and RMSE values of the UO method are decreased by an average of 5.65% (an absolute decrease of 0.0101) and 24.74% (an absolute decrease of 0.0250), respectively.

Table 2 Accuracy assessment of spectral unmixing results for the 10 sites based on correlation coefficient (*R*), root-mean-square-error (RMSE) and mean-absolute-error (MAE) compared to ideal coarse proportions

| Index | Method | Site 1 | Site 2 | Site 3 | Site 4 | Site 5 | Site 6 | Site 7 | Site 8 | Site 9 | Site 10 |
|---|---|---|---|---|---|---|---|---|---|---|---|
| | FCM | 0.9416 | 0.8605 | 0.8266 | 0.8030 | 0.8656 | 0.9092 | 0.8595 | 0.8982 | 0.8665 | 0.9112 |
| | LSMM | 0.9551 | 0.8875 | 0.8398 | 0.8778 | 0.9111 | 0.9162 | 0.8895 | 0.9255 | 0.8760 | 0.9191 |
| *R* | UO | 0.9663 | 0.9161 | 0.8518 | 0.8807 | 0.9127 | 0.9206 | 0.9012 | 0.9297 | 0.8936 | 0.9344 |
| | **UO than FCM** | **0.0247** | **0.0556** | **0.0252** | **0.0777** | **0.0471** | **0.0114** | **0.0417** | **0.0315** | **0.0271** | **0.0232** |
| | **UO than LSMM** | **0.0112** | **0.0286** | **0.0120** | **0.0029** | **0.0016** | **0.0044** | **0.0117** | **0.0042** | **0.0176** | **0.0153** |
| | FCM | 0.1456 | 0.2187 | 0.2272 | 0.2238 | 0.2126 | 0.1813 | 0.2056 | 0.1912 | 0.2035 | 0.1706 |
| | LSMM | 0.1315 | 0.1928 | 0.2177 | 0.1795 | 0.1747 | 0.1739 | 0.1838 | 0.1648 | 0.1970 | 0.1635 |
| RMSE | UO | 0.1135 | 0.1671 | 0.2102 | 0.1797 | 0.1736 | 0.1698 | 0.1732 | 0.1613 | 0.1835 | 0.1467 |
| | **UO than FCM** | **-0.0321** | **-0.0516** | **-0.017** | **-0.0440** | **-0.039** | **-0.0115** | **-0.0324** | **-0.0299** | **-0.0200** | **-0.0239** |
| | **UO than LSMM** | **-0.0180** | **-0.0257** | **-0.0075** | **0.0002** | **-0.0011** | **-0.0041** | **-0.0106** | **-0.0035** | **-0.0135** | **-0.0168** |
| | FCM | 0.0828 | 0.1423 | 0.1465 | 0.1388 | 0.147 | 0.1146 | 0.1264 | 0.1147 | 0.1105 | 0.0898 |
| | LSMM | 0.0801 | 0.1045 | 0.1300 | 0.1011 | 0.1062 | 0.1017 | 0.1033 | 0.0895 | 0.1085 | 0.0854 |
| MAE | UO | 0.0483 | 0.0652 | 0.1051 | 0.0920 | 0.0865 | 0.0794 | 0.0785 | 0.0696 | 0.0798 | 0.0560 |
| | **UO than FCM** | **-0.0345** | **-0.0771** | **-0.0414** | **-0.0468** | **-0.0605** | **-0.0352** | **-0.0479** | **-0.0451** | **-0.0307** | **-0.0338** |
| | **UO than LSMM** | **-0.0318** | **-0.0393** | **-0.0249** | **-0.0091** | **-0.0197** | **-0.0223** | **-0.0248** | **-0.0199** | **-0.0287** | **-0.0294** |

Since the aim of the UO strategy is to reduce spectral unmixing errors by identifying mixed and pure pixels, the mixed and pure pixels are assessed separately. Fig. 7 illustrates these assessments on the 10 sites based on the *R* and RMSE between the coarse proportions and ideal proportions. As shown in Fig. 7, the UO strategy generally produces the largest *R* and the smallest RMSE among the three methods for both the mixed and pure pixels. Further, UO is more advantageous for pure pixels, producing a larger *R* and smaller RMSE compared to those in mixed pixels. Specifically, compared to LSMM, the *R* value is increased by an average of 0.14% and the RMSE value is decreased by an average of 0.52% in mixed pixels across the 10 sites. For pure pixels, the *R* value is increased by an average of 1.32% and the RMSE value is decreased by an average of 15.79% across the 10 sites. This suggests that the segmentation step can effectively reduce the likelihood for pure pixels to be misidentified as mixed pixels.

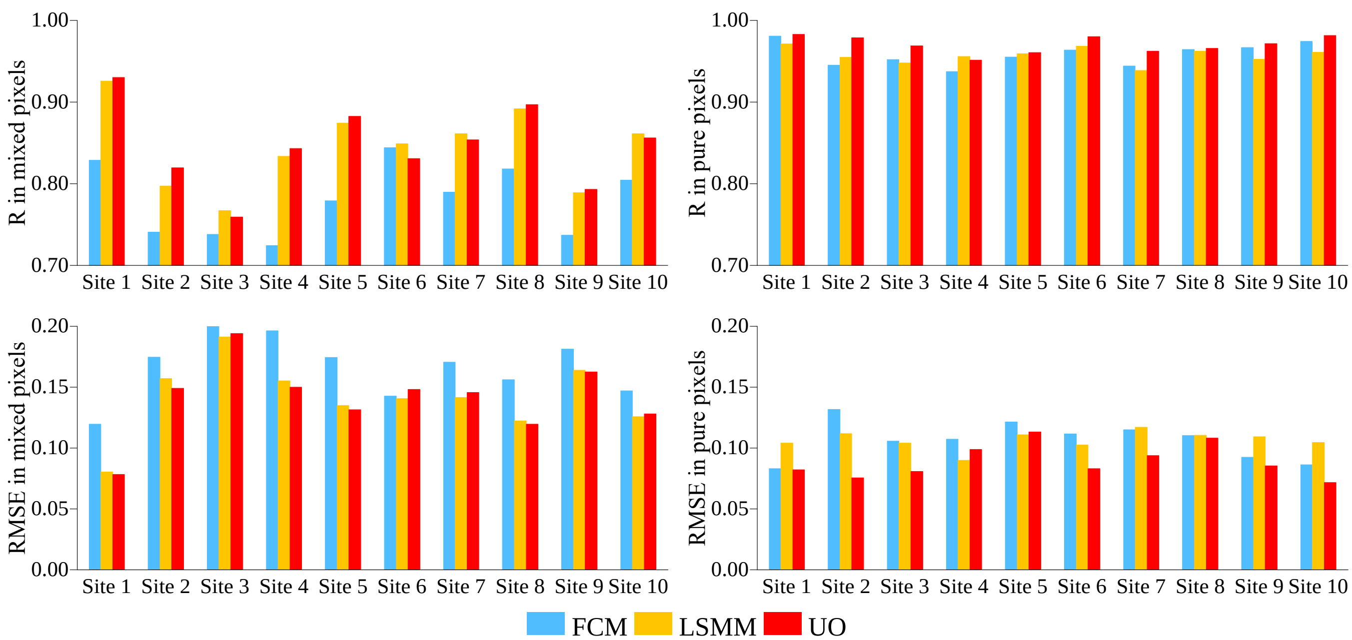


Fig. 7. Correlation coefficient (*R*) and root-mean-square-error (RMSE) of coarse proportions in mixed and pure pixels compared to the corresponding ideal coarse proportions for the 10 study sites.

## *3.4. SPM results*

As a general model, UO-SPM was evaluated in four forms, that is by combining with four SPM methods, namely UO-HNN, UO-MRF, UO-PSA and UO-RBF. Simultaneously, six standard SPM methods (HNN, MRF, PSA, RBF, MFFR-open and MFFR-erode) were applied to two types of coarse proportions obtained by the FCM and LSMM method to provide 12 benchmarks for the UO-SPM results. Figs. 8-10 display the 16 SPM results, with a zoom factor of eight for site 1 and of three for sites 4 and 9. The zoomed coarse images for the three sites are also depicted in Figs. 8-10.

Firstly, the results of the UO-based methods (i.e., UO-HNN, UO-MRF, UO-PSA and UO-RBF, see line 4 of Figs. 8-10) that consider proportions based on object-based analysis, exhibit a significantly closer alignment with the reference images compared to those of the FCM- and LSMM-based methods (i.e., methods prefixed with FCM and LSMM, see lines 2-3 of Figs. 8-10). Specifically, the UO-based methods demonstrate remarkable improvements in restoring large-sized objects with more continuous boundaries, and exhibit fewer speckle artifacts for all datasets, as seen in the zoomed images of Figs. 8-10. Additionally, the LSMM-based methods can generate more details of small objects than the FCM-based methods, but at the cost of producing scattered noise. Overall, the proposed UO-SPM framework is effective for the various SPM methods, outperforming the original SPM methods that use FCM- and LSMM-derived proportions.

Secondly, with the same spectral unmixing methods, the HNN- and MRF-based methods present smoother and visually more appealing results than those of the PSA-, RBF- and MFFR-based methods, while the PSA-, RBF- and MFFR-based methods tend to produce speckle-like artifacts, especially at the boundaries of objects. This because the MRF and HNN can eliminate small amounts of noise through the spatial smoothing term without perfectly conforming to the coarse proportions. It is noteworthy that, through object-based analysis, the UO-PSA and UO-RBF methods also mitigate errors obviously in the inner parts of objects compared to the results of LSMM-PSA and LSMM-RBF. Moreover, although morphological operations were considered in the MFFR method, the refilling process of MFFR still complies to the coarse proportions. Overall, as errors in spectral unmixing are inevitable in real applications, the UO-MRF and UO-HNN would be more suitable for land cover mapping among the 16 SPM methods in practice.

In conclusion, all of the UO-SPM-based methods reconstruct more accurate results than the FCM- and LSMM-based versions for both large-sized and small-sized land cover classes. Furthermore, the comparison between different SPM methods reveals that the SPM methods strictly satisfying the coarse proportion constraints (i.e., PSA and RBF) can be notably enhanced within the UO-SPM framework. Meanwhile, the UO-MRF and UO-HNN produce visually more accurate predictions than PSA, RBF and MFFR-based methods.

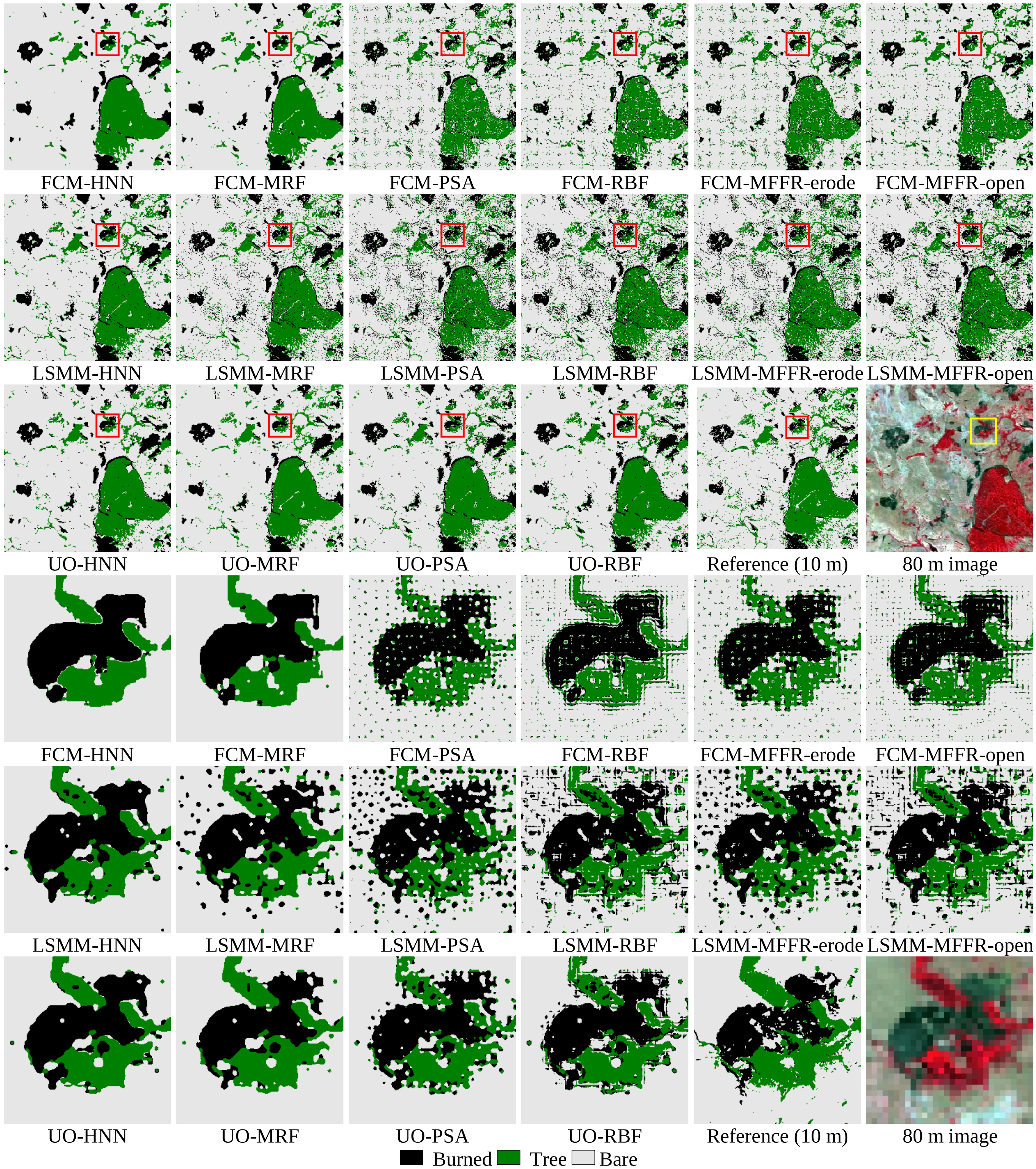


Fig. 8. SPM results for Site 1 (with a zoomed subarea in the last three lines).

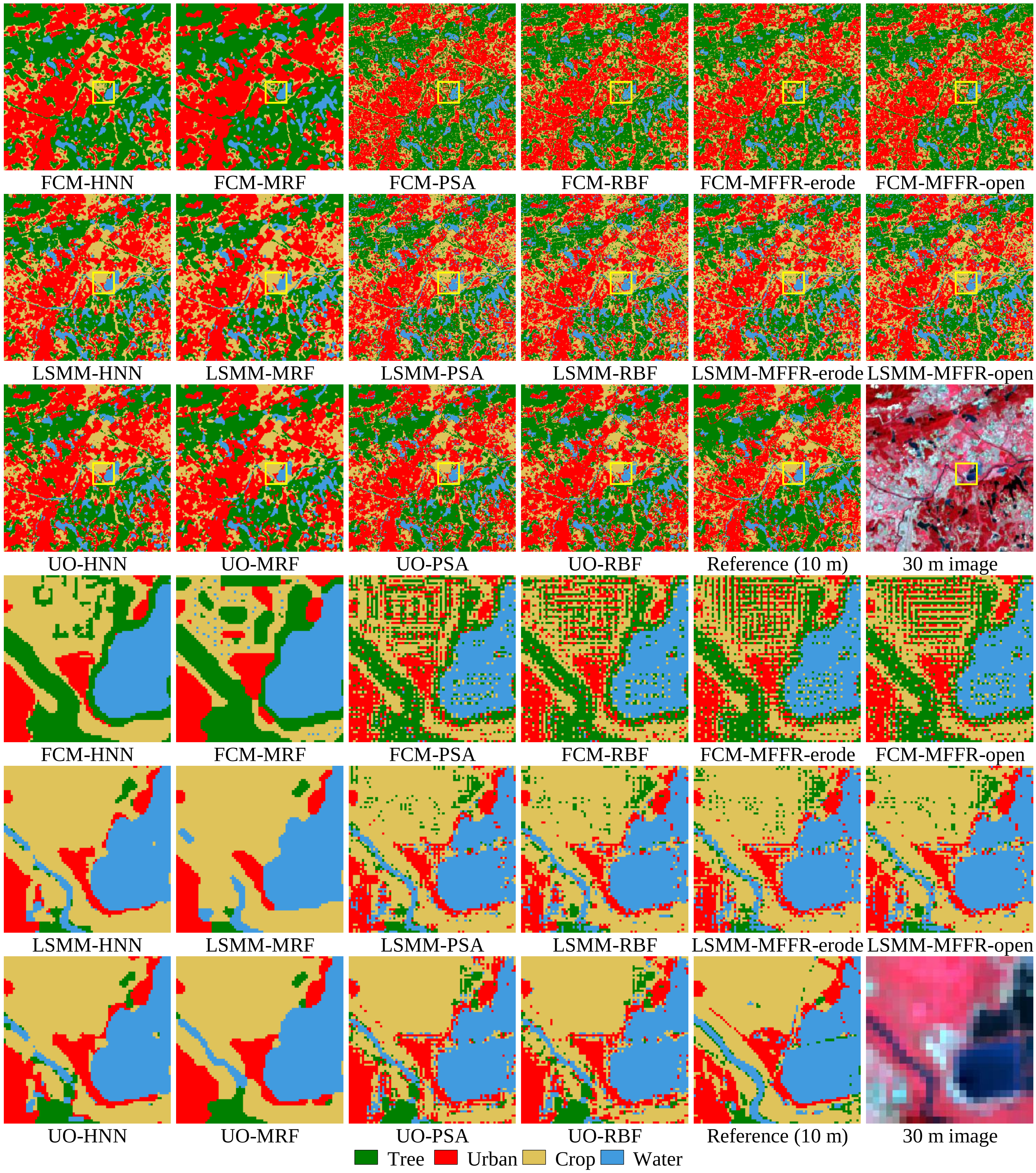


Fig. 9. SPM results for Site 4 (with a zoomed subarea in the last three lines).

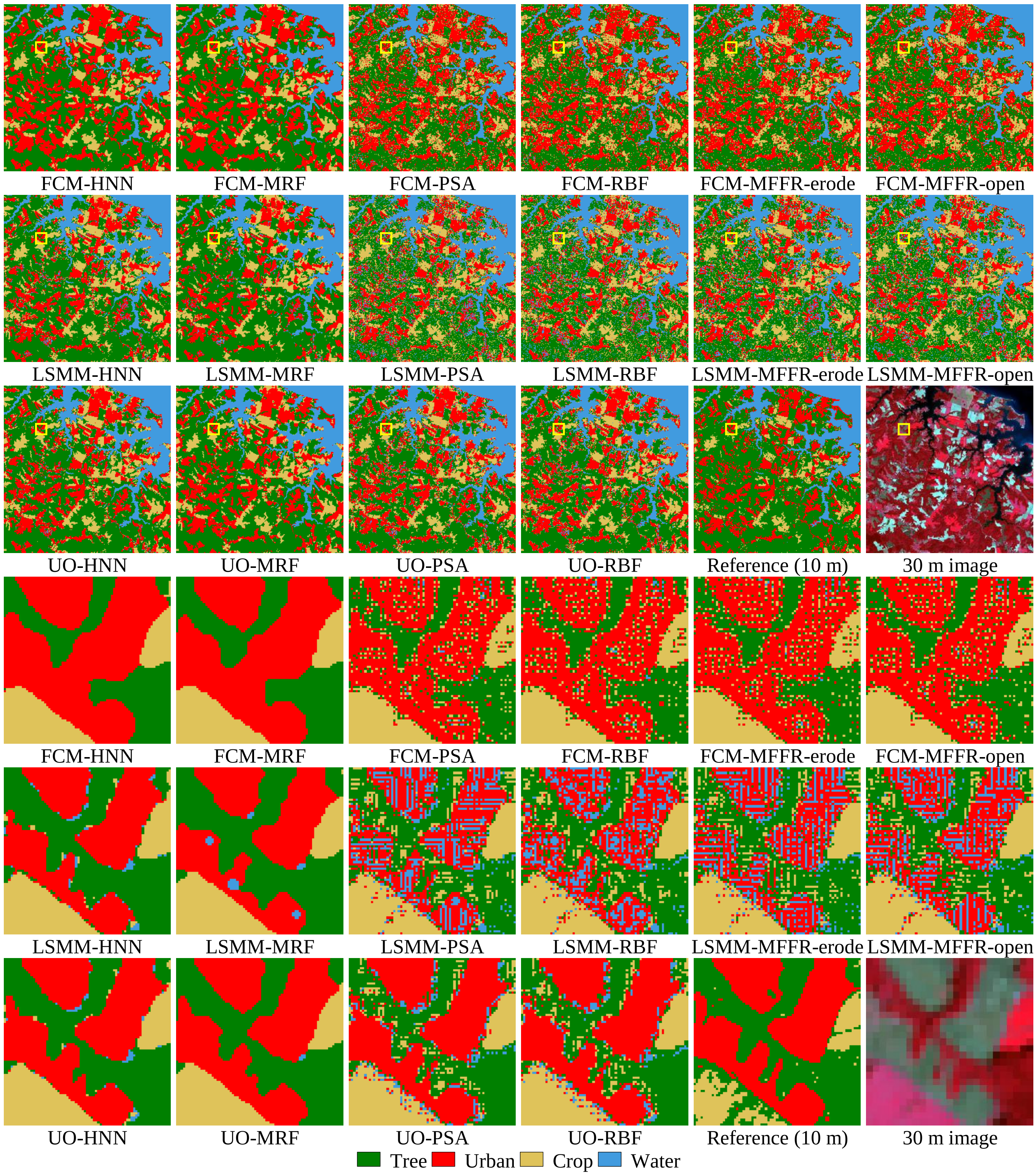


Fig. 10. SPM results for Site 9 (with a zoomed subarea in the last three lines).

Table 3 Overall accuracy (OA) of SPM results for the 10 sites

| | Methods | HNN | MRF | PSA | RBF | MFFR-erode | MFFR-open |
|---|---|---|---|---|---|---|---|
| Site 1 | FCM-SPM | 0.8949 | 0.9058 | 0.8385 | 0.8414 | 0.8387 | 0.8408 |
| | LSMM-SPM | 0.9154 | 0.8864 | 0.8344 | 0.8387 | 0.8344 | 0.8375 |
| | UO-SPM | 0.9176 | **0.9211** | 0.9028 | 0.9050 | | |
| Site 2 | FCM-SPM | 0.8545 | 0.8665 | 0.7061 | 0.7092 | 0.7079 | 0.7077 |
| | LSMM-SPM | 0.8766 | 0.8814 | 0.7801 | 0.7811 | 0.7796 | 0.7805 |
| | UO-SPM | 0.8933 | **0.8977** | 0.8590 | 0.8593 | | |
| Site 3 | FCM-SPM | 0.8020 | 0.8189 | 0.6775 | 0.6765 | 0.6752 | 0.6748 |
| | LSMM-SPM | 0.8148 | 0.8321 | 0.7158 | 0.7199 | 0.7122 | 0.7155 |
| | UO-SPM | 0.8183 | **0.8385** | 0.7686 | 0.7714 | | |
| Site 4 | FCM-SPM | 0.7354 | 0.7230 | 0.6620 | 0.6637 | 0.6578 | 0.6592 |
| | LSMM-SPM | 0.7950 | 0.7889 | 0.7436 | 0.7448 | 0.7343 | 0.7401 |
| | UO-SPM | **0.7954** | 0.7920 | 0.7664 | 0.7665 | | |
| Site5 | FCM-SPM | 0.8239 | 0.8334 | 0.7266 | 0.7302 | 0.7260 | 0.7270 |
| | LSMM-SPM | 0.8582 | 0.8465 | 0.7943 | 0.7959 | 0.7262 | 0.7269 |
| | UO-SPM | **0.8603** | 0.8554 | 0.8341 | 0.8348 | | |
| Site 6 | FCM-SPM | 0.8672 | 0.8763 | 0.7895 | 0.7919 | 0.7885 | 0.7896 |
| | LSMM-SPM | 0.8834 | 0.8809 | 0.8108 | 0.8113 | 0.7885 | 0.7896 |
| | UO-SPM | 0.8790 | **0.8861** | 0.8544 | 0.8542 | | |
| Site 7 | FCM-SPM | 0.8261 | 0.8338 | 0.7147 | 0.7168 | 0.7126 | 0.7133 |
| | LSMM-SPM | 0.8575 | 0.8130 | 0.7690 | 0.7701 | 0.7598 | 0.7653 |
| | UO-SPM | 0.8621 | **0.8649** | 0.8216 | 0.8227 | | |
| Site 8 | FCM-SPM | 0.8584 | 0.8700 | 0.7903 | 0.7934 | 0.7898 | 0.7906 |
| | LSMM-SPM | 0.8820 | 0.8836 | 0.8326 | 0.8347 | 0.8267 | 0.8315 |
| | UO-SPM | 0.8882 | **0.8902** | 0.8729 | 0.8736 | | |
| Site 9 | FCM-SPM | 0.8336 | 0.8489 | 0.7585 | 0.7590 | 0.7577 | 0.7580 |
| | LSMM-SPM | 0.8507 | 0.8693 | 0.7639 | 0.7644 | 0.7597 | 0.7622 |
| | UO-SPM | 0.8571 | **0.8657** | 0.8241 | 0.8238 | | |
| Site 10 | FCM-SPM | 0.8766 | 0.8852 | 0.8131 | 0.8151 | 0.8118 | 0.8129 |
| | LSMM-SPM | 0.8944 | 0.9049 | 0.8149 | 0.8164 | 0.8117 | 0.8140 |
| | UO-SPM | 0.9047 | **0.9129** | 0.8764 | 0.8766 | | |

Table 3 lists the overall accuracy (OA) of the SPM methods combined with the FCM, LSMM and UO-derived proportions, delineated line-by-line for the 10 sites. Across all experiments, the OA values of UO-SPM consistently surpass those of the FCM and LSMM-based methods. Specifically, the OAs of the UO-PSA and UO-RBF methods exceed those of the FCM-PSA and LSMM-RBF by an average of about 9% and surpass those of the LSMM-PSA and LSMM-RBF by an average of about 5% for the 10 sites. Although the enhancement is less pronounced for the HNN and MRF methods, there is still an increase in OA compared to the results of the FCM-based and LSMM-based methods. More precisely, the OA of the UO-MRF method exceeds those of FCM-MRF and LSMM-MRF by 2.63% and 1.38%, respectively. For HNN, the OA of UO-HNN is 3.03% and 0.48% larger than FCM-HNN and LSMM-HNN, respectively. Furthermore, the UO-MRF produces the largest OA among all methods, with an average of 87.25%. The MFFR-erode and

MFFR-open methods exhibit OAs similar to RBF and PSA. Overall, the UO-SPM model is demonstrated to be effective for all four SPM methods, achieving larger OAs compared to the original methods with both the FCM and LSMM-derived proportions.

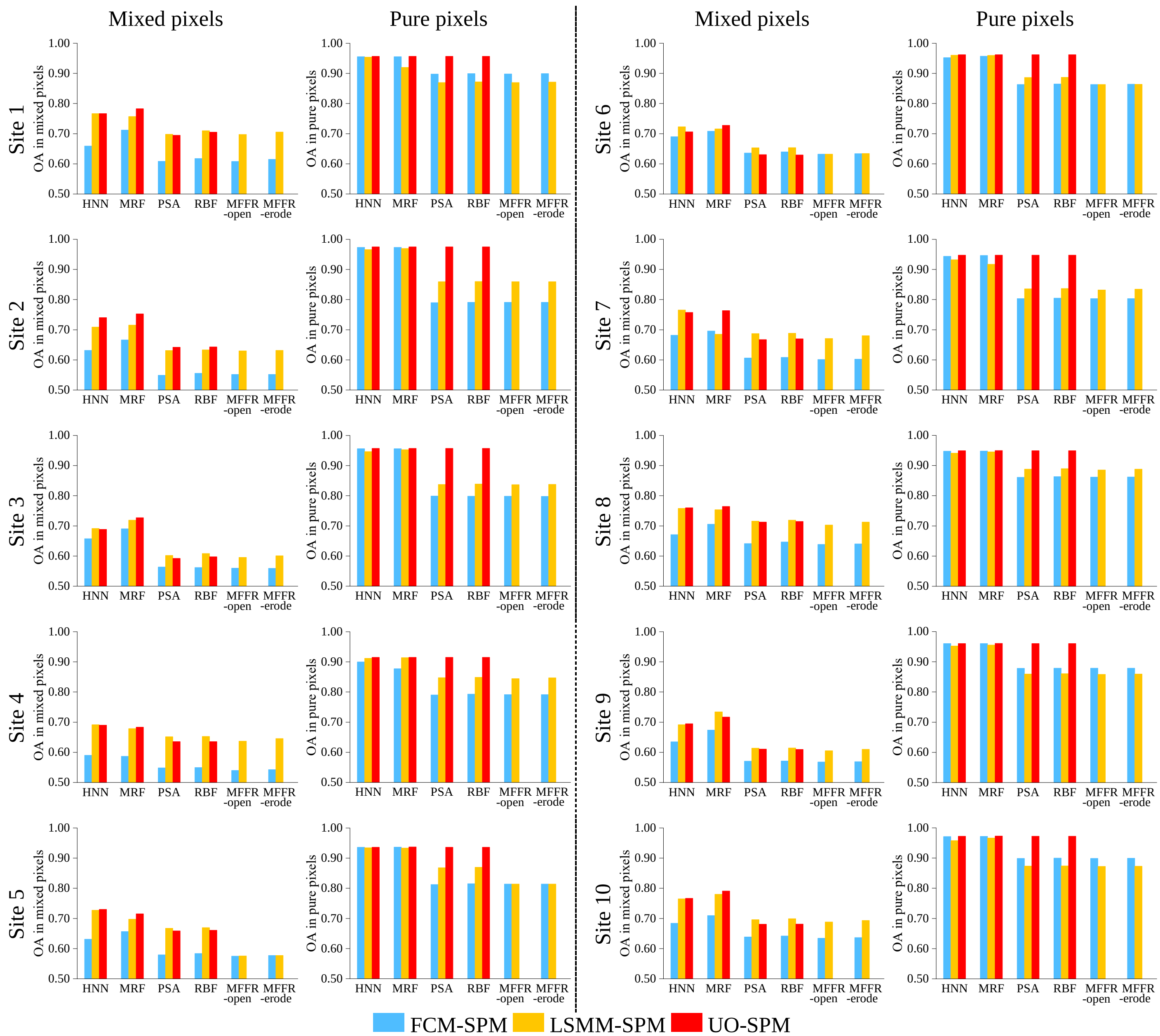


Fig. 11. Classification accuracies (in terms of OA) for mixed pixels and pure pixels for the 10 sites.

As pure and mixed pixels are handled differently in the SPM process, the accuracies of the two types of pixels are analyzed separately for the 10 sites, as shown in Fig. 11. Incorporation of the UO-SPM model results in an observable increase in OA for both mixed and pure pixels. This increase is more apparent for mixed pixels in the case of UO-HNN and UO-MRF, while for UO-PSA and UO-RBF, the enhancement is more apparent for pure pixels than for mixed pixels. For example, compared to FCM-HNN, the accuracies of mixed pixels are increased by 10.72%, 10.85% and 3.11%, and those of pure pixels by 0.09%, 0.15% and 0.07% for sites 1-3, respectively. Moreover, the OAs for mixed pixels are generally smaller than for pure pixels, reflecting the difficulty, but also importance, of addressing the mixed pixel problem.

# 4. Discussion

## *4.1. Consideration of unsupervised FCM*

Since the initial step of UO-SPM involves unsupervised FCM, the reliability of the FCM results warrants consideration. In the proposed UO-SPM model, initial FCM-derived coarse proportions are used to identify mixed and pure pixels through a segmentation-then-erosion step, followed by secondary LSMM-based unmixing of the remaining mixed pixels using endmembers extracted by averaging the spectral values of all filtered pure pixels (i.e., a global LSMM strategy that uses the same endmembers for all pixels). Thus, the initial FCM step might affect the identification of mixed and pure pixels and subsequently affect the accuracy of secondary spectral unmixing. To evaluate this, the spectral unmixing results of the original UO strategy were compared to two other versions, as listed in Table 4. Specifically, 'FCM-global' denotes the original UO strategy that conducts the segmentation-then-erosion step on the FCM-derived coarse proportions, followed by global LSMM for the remaining mixed pixels (i.e., the proposed scheme). 'LSMM-global' involves conducting the segmentation-then-erosion step on the LSMM-derived coarse proportions and then decomposing the identified mixed pixels using global LSMM. 'FCM-local' denotes conducting a segmentation-then-erosion step on the FCM results, followed by local LSMM that uses different endmembers for each pixel, which are extracted from its surrounding pure pixels.

Table 4 Comparison of three spectral unmixing strategies based on the *R*, RMSE and MAE between the results and ideal coarse proportions for the 10 sites

| Index | Method | Site 1 | Site 2 | Site 3 | Site 4 | Site 5 | Site 6 | Site 7 | Site 8 | Site 9 | Site 10 | Average |
|---|---|---|---|---|---|---|---|---|---|---|---|---|
| | FCM-global (proposed) | 0.9663 | 0.9161 | 0.8518 | 0.8807 | 0.9127 | 0.9206 | 0.9012 | 0.9297 | 0.8936 | 0.9344 | 0.9107 |
| *R* | LSMM-global | 0.9697 | 0.9243 | 0.8397 | 0.8857 | 0.9130 | 0.9254 | 0.9045 | 0.9299 | 0.8917 | 0.9301 | 0.9114 |
| | FCM-local | 0.9673 | 0.9189 | 0.8515 | 0.8778 | 0.9098 | 0.9182 | 0.8992 | 0.9294 | 0.8919 | 0.9338 | 0.9098 |
| | FCM-UO | 0.1135 | 0.1671 | 0.2102 | 0.1797 | 0.1736 | 0.1698 | 0.1732 | 0.1613 | 0.1835 | 0.1467 | 0.1679 |
| RMSE | LSMM-global | 0.1057 | 0.1590 | 0.2180 | 0.1741 | 0.1725 | 0.1637 | 0.1703 | 0.1600 | 0.1846 | 0.1513 | 0.1659 |
| | FCM-local | 0.1122 | 0.1645 | 0.2104 | 0.1816 | 0.1765 | 0.1724 | 0.1750 | 0.1607 | 0.1849 | 0.1474 | 0.1686 |
| | FCM-global (proposed) | 0.0483 | 0.0652 | 0.1051 | 0.0920 | 0.0865 | 0.0794 | 0.0785 | 0.0696 | 0.0798 | 0.0560 | 0.0760 |
| MAE | LSMM-global | 0.0487 | 0.0598 | 0.1092 | 0.0939 | 0.0878 | 0.0803 | 0.0838 | 0.0727 | 0.0832 | 0.0576 | 0.0777 |
| | FCM-local | 0.0467 | 0.0623 | 0.1046 | 0.0934 | 0.0881 | 0.0803 | 0.0791 | 0.0694 | 0.0804 | 0.0560 | 0.0760 |

As observed in Table 4, the difference between the ‘LSMM-global’ and ‘FCM-global’ results is small, with a difference of 0.07% in average *R*, indicating that the segmentation-then-erosion step in the proposed UO model reduces the errors in the FCM-derived coarse proportions effectively. Additionally, the ‘FCM-local’ method produces accuracy comparable to the ‘FCM-global’ method, since the difference between them is only in the unmixing of the filtered mixed pixels. Overall, despite being an unsupervised approach, the proposed ‘FCM-global’ strategy achieves relatively satisfactory coarse proportions and can contribute to more accurate SPM results.

### *4.2. Alternatives to segmentation algorithm*

To tackle the mixed pixel problem, pixel-based analysis is employed widely in current spectral unmixing and SPM. However, the pre-spectral unmixing process introduces inevitable uncertainties, affecting not only mixed pixels, but also leading to misidentification of pure pixels due to intra-class and inter-class spectral variability issues. This is a common limitation in many existing SPM methods that rely on coarse proportions as a data fidelity term. In this paper, the UO-SPM model incorporates the Otsu-based segmentation method to divide the coarse proportions of each land cover class into targets (more likely to be pure pixels of one class) and backgrounds (more likely to be mixed pixels or pure pixels for other classes). With the goal of minimizing intra-class variance, the Otsu algorithm is appropriate for segmenting the coarse proportions that generally exhibit an obvious two peaks-distributed histogram. Otsu may not be optimal under every circumstance, such as when the coarse proportion is significantly affected by noise, or when there is a considerable area difference between the target and background. Nevertheless, it is widely acknowledged that there is no perfect algorithm that will work with every satellite sensor image (Kotaridis and Lazaridou, 2021). Alternative segmentation algorithms, such as edge detection and region merging, may demonstrate better performance than Otsu in specific scenarios. Regarding these methods, it must be noted that the selection of parameters should be done carefully, as the choice will impact directly on the segmentation output.

In the UO-SPM model, Otsu has the obvious advantage of automatic threshold selection without the need for parameters or supervision, making it ideal for integration into the proposed unsupervised models. Moreover, the main goal of employing segmentation is utilization of object-oriented contextual information to differentiate mixed and pure pixels from the coarse proportions. This enables the exclusion of noisy errors in the pure pixels while simultaneously obtaining more accurate spectral unmixing for the mixed pixels by application of a secondary supervised spectral unmixing step. Therefore, the key to UO-SPM is not which segmentation method is used, but the appropriate use of spatial contextual information through an object-based analysis, a consideration lacking in conventional pixel-based spectral unmixing and SPM.

### *4.3. Ideal width of mixed pixel*

Ideally, the width of mixed pixels is expected to be one coarse pixel, corresponding to the edge pixels at the intersection of two land cover objects. In the UO-SPM experiments, the size of the structuring element in the morphological erosion step was set to three. This decision was made considering the challenges posed by errors in the pre-spectral unmixing process and uncertainties in the segmentation results, making it difficult to identify precisely the one-pixel width of mixed pixel positions. If the morphological erosion step is set too small, it could result in a substantial omission error for the mixed pixels. To investigate the impact of different sizes of the structuring element in the erosion step, we examined the UO-based spectral unmixing result using elements with a size of 1, 2, 3, 5 and 7 pixels for the 10 study sites. The average $R$ values (for the 10 sites) of the

UO-derived coarse proportions with different sizes of structuring elements are shown in Fig. 12. It can be seen that the average *R* values for all pixels and mixed pixels increase initially and then decrease as the size of the structuring element increases. Additionally, the *R* values for pure pixels tend to decrease when the size of structuring element exceeds three. Furthermore, the difference in the average *R* values between the results of UO with different structuring sizes is less than 1.2% for all pixels. Overall, while the proposed UO model requires setting the parameter of the structuring element, it demonstrates satisfactory performance with a setting of three, as evaluated across the 10 sites. Hence, a size of 3 pixels for the structuring element is suggested for the proposed UO-SPM model.

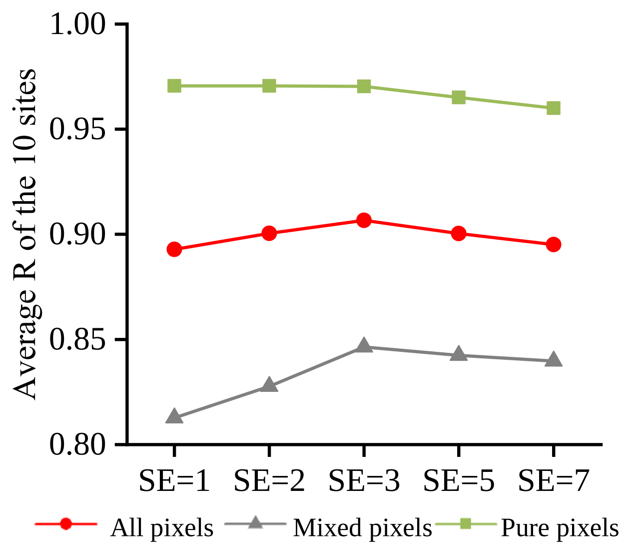


Fig. 12. Assessment of the impact of the size of the structuring element (SE) on the UO-derived spectral unmixing results for the 10 study sites.

*4.4. Limitations of UO-SPM*

With the object-scale analysis, the proposed UO-SPM model leverages contextual relations that a single pixel view lacks. The underlying assumption of UO-SPM is that land cover objects are large-sized, typically larger than one coarse pixel (i.e., a H-resolution case) (Atkinson, 2009). For example, in a Landsat image with a spatial resolution of 30 m, the proposed UO-SPM requires objects to be larger than 90 m × 90 m (i.e., 3×3 Landsat pixels) to identify ideal pure pixels using a structuring size of three for erosion. This makes the method more suitable for homogeneous areas. However, this does not follow that the method is not applicable to small-sized land covers, as they may be identified as mixed pixels after the erosion step and then are decomposed to obtain coarse proportions. To assess the discrepancies in accuracies between the H-resolution and L-resolution cases, the edge density (ED) of the 10 study sites was calculated from the reference land cover maps by dividing the total edge length by the total area. Specifically, the number of pixels at the edges is viewed as the total edge length, while the total number of pixels is considered as the total area. That is, the unit of ED here is the number of edge pixels per pixel. A larger edge density indicates a more complex and fragmented landscape (Clément et al., 2017), representing more L-resolution cases in the coarse image, while smaller edge density suggests more contiguous patches, representing more H-resolution cases.

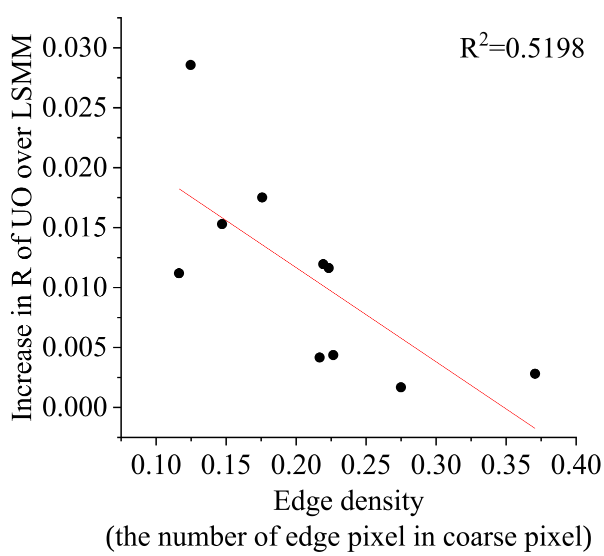


Fig. 13. The relationship between the edge density (ED) of the reference land cover images and the increase in *R* value of the UO-derived coarse proportions compared to the LSMM-derived results for the 10 sites (a larger edge density represents a more fragmented landscape, more likely indicating an L-resolution case in the coarse image).

The relationship between ED and the increase in *R* of the UO-derived coarse proportions compared to LSMM for the 10 sites is shown in Fig. 13. With less fragmented objects (i.e., smaller ED value), the advantage of the UO-strategy over LSMM is more evident. This suggests that the proposed method is more suitable for the H-resolution case. The reason is that when the size of target object is small, as in the L-resolution case, the effectiveness of the object-scale analysis diminishes in detecting objects within the coarse pixel, further affecting the performance of spectral unmixing and SPM. Since there is no guidance on predicting the fine land cover distribution within a coarse pixel, for such pixels, if they were correctly segmented as backgrounds by the proposed UO-SPM model for all classes (i.e., remaining mixed pixels), they would be further decomposed in the secondary spectral unmixing step. Conversely, if such pixels were erroneously segmented as pure pixels for one class, the error would propagate into the SPM results. To overcome the challenge of small-sized objects (particularly for those falling entirely within a coarse pixel), the utilization of auxiliary data, such as fine spatial resolution temporally adjacent land cover maps, should be a potential approach. Additionally, to effectively identify objects in Landsat images using UO-SPM, the classification system should be defined at a higher representation level. For example, finding pure pixels for asphalt, concrete and roofing materials within 'urban areas' in Landsat images can be challenging. Therefore, it is reasonable to group these materials into a single category, such as an 'urban' class, as is commonly adopted in existing global land cover products based on Sentinel-2 and Landsat images (Zhang et al., 2021; Brown et al., 2022). Under such a classification system, regions can be considered relatively homogeneous with significant intra-class variance at the pixel scale. In this scenario, the object-based analysis in UO-SPM offers great advantages compared to pixel-based strategies for addressing such intra-class variance.

### *4.5. Applicability to scenes with a large number of classes*

Due to the limited number of spectral bands in multi-spectral images, spectral unmixing methods face inherent challenges in capturing sufficient spectral information to differentiate between a large number of land cover classes. For example, decomposing different types of vegetation, such as trees and shrubs, becomes difficult with only a few spectral bands due to their spectral similarity. Additionally, linear unmixing methods (e.g., LSMM) become more suitable when the number of classes is smaller than the number of bands. In the experiments in Section 3, the proposed UO model was applied to multi-spectral images using a relatively coarse land cover taxonomy with limited spectral bands. When sufficient spectral bands are available to differentiate land cover classes, such as hyperspectral images, coarse proportions can be obtained more readily.

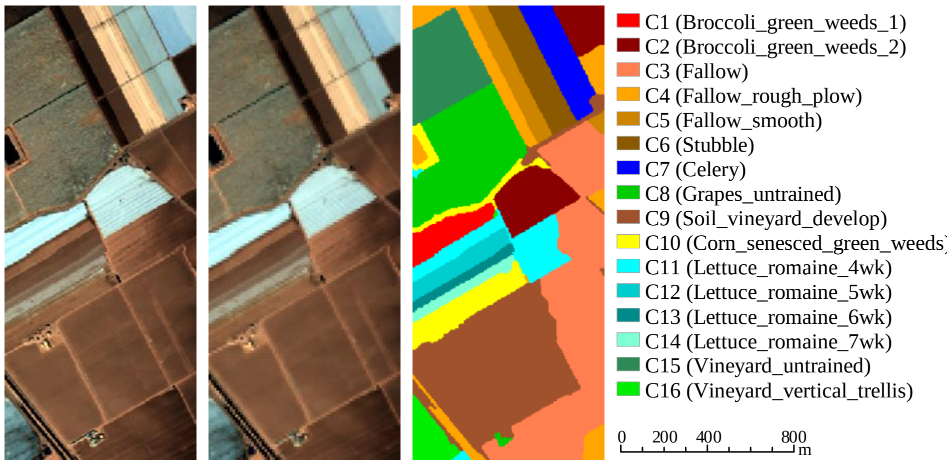


(a) (b) (c)

Fig. 14. The hyperspectral Salinas AVIRIS dataset with 16 classes. (a) Original 3.7 m image (Bands 90, 65 and 55 as RGB). (b) Simulated 11.1 m coarse image obtained by degrading (a) with a scale factor of 3. (c) 3.7 m land cover map produced by Zhao et al. (2020).

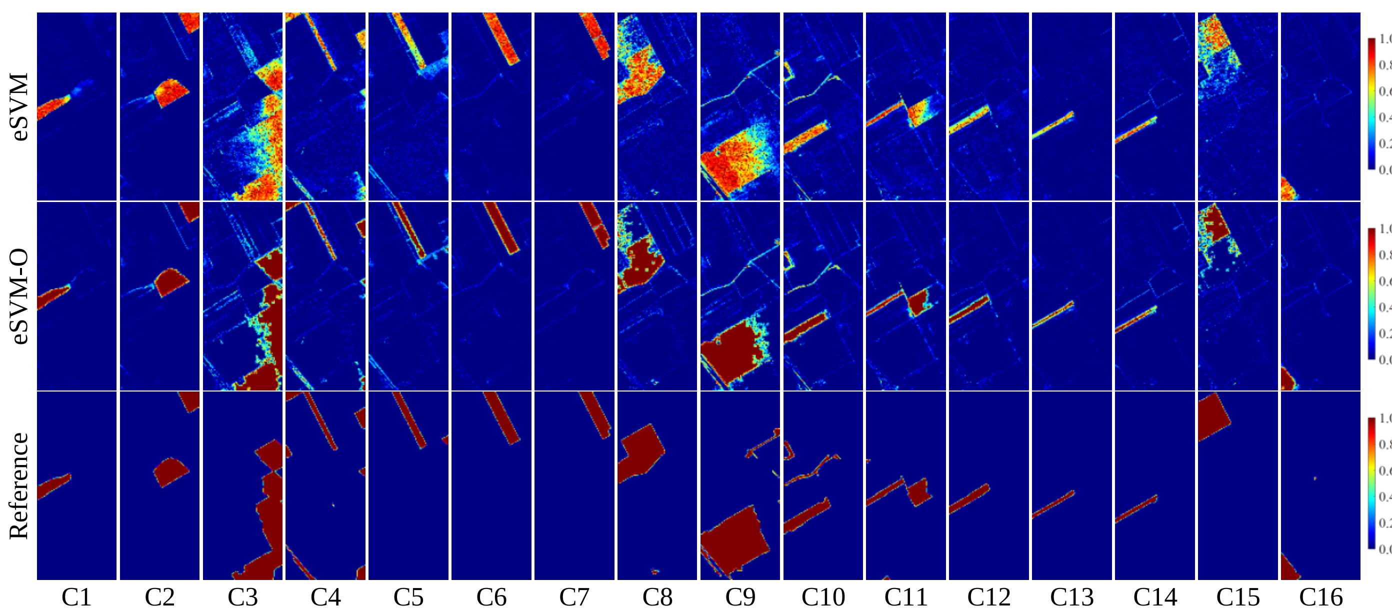


Fig. 15. Spectral unmixing results for the 11.1 m hyperspectral Salinas AVIRIS dataset.

To evaluate the potential of the proposed object-based analysis in scenes with a large number of land cover classes, a hyperspectral image acquired by the Airborne/Visible Infrared Imaging Spectrometer (AVIRIS) sensor was used, as shown in Fig. 14. The image was captured over Salinas Valley in California, USA, and contains 204 spectral bands (after noise removal) between 0.4 and 2.5 μm, with a spatial resolution of 3.7 m and spatial size of 510 × 210 pixels. The original 3.7 m hyperspectral image was degraded to 11.1 m to simulate the coarse image for spectral unmixing, as shown in Fig. 14(b). The 3.7 m land cover map in Fig. 14(c) was generated by the method developed in Zhao et al. (2020), and has an OA of 99.40% when compared to the available ground reference data. Similarly, the reference for 11.1 m coarse proportions was produced by degrading Fig. 14(c) with a scale factor of 3. Here, for spectral unmixing, the unsupervised FCM method was not considered, as several land cover classes cannot be identified when the number of land cover classes is large. The proposed UO scheme was also extended to cope with the challenging case in this section. Specifically, a supervised spectral unmixing method called extended SVM (eSVM) (Li et al., 2015) was employed to replace FCM in the proposed method. The eSVM decomposes mixed pixels by considering their proximity to the class cores of pure endmembers, without making hard label decisions. Accordingly, two supervised spectral unmixing methods were implemented, including eSVM and eSVM-O. For the eSVM method, we selected randomly 10% of the pure pixels from each land cover class in the reference coarse proportion images as training samples to predict the remaining pixels. For eSVM-O, the segmentation-then-erosion step with a structuring size of 3 for erosion was applied to the eSVM-derived proportions, while the remaining mixed pixels inherited the eSVM-derived proportions directly. Visual inspection in Fig. 15 shows that compared to the results of eSVM, the eSVM-O reduces the errors noticeably in the inner regions of objects, and the results are obviously closer to the reference. As listed in Table 5, the quantitative evaluations based on $R$, RMSE and MAE align with the visual comparison. Furthermore, the two coarse proportions were used as inputs to the SPM methods (including HNN, MRF, PSA and RBF) to generate the 3.7 m spatial resolution maps. The results are shown in Fig. 16, and the accuracy assessment is provided in Table 6. It can be seen that the SPM predictions show obvious reduction in errors both visually and quantitatively when using proportions derived from eSVM-O. Overall, when sufficient spectral bands are available to distinguish between a large number of land cover classes, such as in hyperspectral images, the object-based analysis proposed in this paper is helpful to further enhance the unmixing results and, eventually, to increase the accuracy of SPM predictions.

Table 5 Spectral unmixing accuracies for the hyperspectral Salinas AVIRIS dataset

| | *R* | | RMSE | | MAE | |
|---|---|---|---|---|---|---|
| | eSVM | eSVM-O | eSVM | eSVM-O | eSVM | eSVM-O |
| C1 | 0.9657 | 0.9705 | 0.0463 | 0.0376 | 0.0109 | 0.0055 |
| C2 | 0.9759 | 0.9800 | 0.0631 | 0.0480 | 0.0199 | 0.0096 |
| C3 | 0.8794 | 0.9236 | 0.1959 | 0.1511 | 0.1115 | 0.0519 |
| C4 | 0.8531 | 0.8560 | 0.1293 | 0.1215 | 0.0462 | 0.0301 |
| C5 | 0.8599 | 0.9094 | 0.0910 | 0.0712 | 0.0343 | 0.0179 |
| C6 | 0.9796 | 0.9794 | 0.0529 | 0.0416 | 0.0160 | 0.0085 |
| C7 | 0.9770 | 0.9774 | 0.0511 | 0.0421 | 0.0131 | 0.0070 |
| C8 | 0.8624 | 0.8945 | 0.1612 | 0.1386 | 0.0725 | 0.0421 |
| C9 | 0.9099 | 0.9340 | 0.1791 | 0.1415 | 0.0960 | 0.0463 |
| C10 | 0.8740 | 0.8811 | 0.1113 | 0.1022 | 0.0410 | 0.0276 |
| C11 | 0.8870 | 0.9146 | 0.0994 | 0.0818 | 0.0387 | 0.0211 |
| C12 | 0.9132 | 0.9456 | 0.0680 | 0.0478 | 0.0245 | 0.0110 |
| C13 | 0.9465 | 0.9493 | 0.0416 | 0.0358 | 0.0110 | 0.0066 |
| C14 | 0.9185 | 0.9266 | 0.0469 | 0.0425 | 0.0139 | 0.0092 |
| C15 | 0.8099 | 0.8507 | 0.1497 | 0.1318 | 0.0605 | 0.0361 |
| C16 | 0.9348 | 0.9385 | 0.0577 | 0.0486 | 0.0147 | 0.0084 |
| Overall | 0.9027 | 0.9249 | 0.1088 | 0.0906 | 0.0390 | 0.0212 |

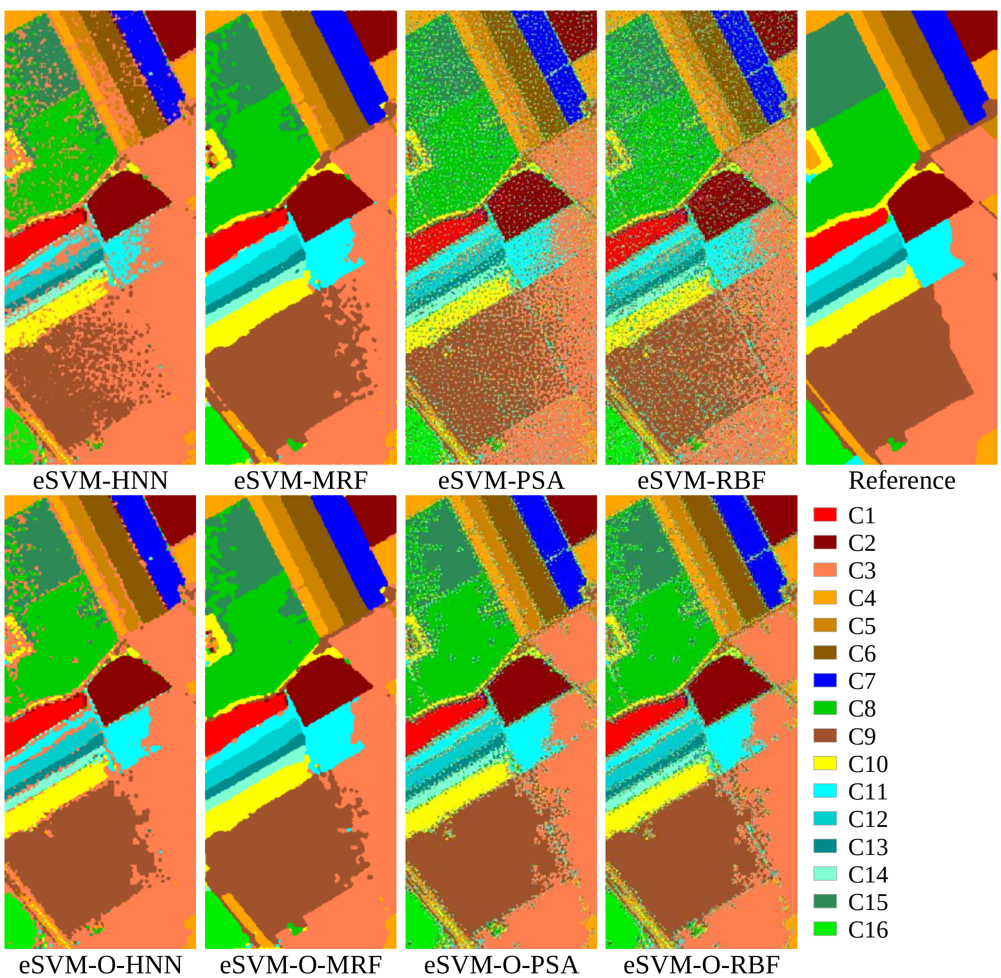


Fig.16. SPM results (3.7 m) for the hyperspectral Salinas AVIRIS dataset.

Table 6 OA of SPM results for the hyperspectral Salinas AVIRIS dataset

| | HNN | MRF | PSA | RBF |
|---|---|---|---|---|
| eSVM-SPM | 76.60% | 91.66% | 68.25% | 68.36% |
| eSVM-O-SPM | 84.68% | 92.03% | 82.56% | 82.49% |

## 5. Conclusion

As a pre-processing step of SPM, spectral unmixing produces coarse proportions, serving as a crucial data fidelity term for various SPM methods, and influencing SPM results greatly. However, widely used pixel-based spectral unmixing methods often introduce inevitable errors due to inherent spectral variability in the observed data. Moreover, pixel-based spectral analysis neglects valuable contextual information on land cover objects, and commonly used supervised-based spectral unmixing methods entail human input, resulting in a heavy labor burden. In this paper, we introduced a fully automatic object-based SPM model, namely UO-SPM, to increase the accuracy of spectral unmixing and ultimately SPM. Given that mixed pixels are often located at the boundaries of land cover classes (i.e., edge of objects), this paper developed an object-scale strategy to identify both mixed and pure pixels. The proposed UO-SPM model was integrated with four SPM methods (i.e., UO-MRF, UO-HNN, UO-PSA and UO-RBF) and evaluated across three multi-spectral datasets. The results were compared with two versions of the existing morphological operation-based SPM method, that is, MFFR-erode and MFFR-open.

The key findings are as follows. Firstly, the proposed UO-SPM model offers an effective solution to reduce errors in spectral unmixing results, subsequently enhancing SPM, with an average increase of 3.65% and 1.09% in $R$ value for coarse proportions compared to FCM and LSMM, respectively. The UO-SPM strategy produced larger accuracies for SPM than the FCM-SPM and LSMM-SPM methods, with an average increase of 5.89% and 3.04% in OA compared to the FCM-SPM and LSMM-SPM results, respectively. Secondly, evaluation of mixed and pure pixels reveals that both are more accurately classified by the UO-SPM model for all SPM methods. The results include fewer erroneous speckle-like subpixels within pure pixels and produce a more satisfactory fine land cover distribution for mixed pixels. Thirdly, the proposed UO-SPM model is applicable for both SPM methods that comply strictly with the coarse proportions (i.e., RBF and PSA) and methods that do not strictly preserve the coarse proportions (i.e., MRF and HNN). The increase in accuracy is more obvious for UO-PSA and UO-RBF than that for UO-MRF and UO-HNN, while UO-MRF produces the most accurate results among all methods. Lastly, the advantage of UO-SPM is more evident for land cover types with large-sized objects than for those with small-sized case. With the aim of detecting mixed pixels located at the edges of objects, the proposed UO-SPM model is more suitable for the H-resolution case than the L-resolution case.

## Acknowledgments

This work was supported by the National Natural Science Foundation of China under Grants 42222108 and 42171345.

## References

Atkinson, P.M. (2005). Sub-pixel target mapping from soft-classified, remotely sensed imagery. *Photogrammetric Engineering & Remote Sensing, 71*, 839-846

Atkinson, P.M. (2009). Issues of uncertainty in super-resolution mapping and their implications for the design of an inter-comparison study. *International Journal of Remote Sensing, 30*, 5293-5308

Auch, R.F., Wellington, D.F., Taylor, J.L., Stehman, S.V., Tollerud, H.J., Brown, J.F., Loveland, T.R., Pengra, B.W., Horton, J.A., Zhu, Z., Midekisa, A.A., Sayler, K.L., Xian, G., Barber, C.P., & Reker, R.R. (2022). Conterminous united states land-cover change (1985-2016): New insights from annual time series. *Land, 11*, 298

Borsoi, R.A., Imbiriba, T., Bermudez, J.C.M., & Richard, C. (2020). A blind multiscale spatial regularization framework for kernel-based spectral unmixing. *IEEE Transactions on Image Processing, 29*, 4965-4979

Borsoi, R.A., Imbiriba, T., Bermudez, J.C.M., Richard, C., Chanussot, J., Drumetz, L., Tourneret, J.-Y., Zare, A., & Jutten, C. (2021). Spectral variability in hyperspectral data unmixing: A comprehensive review. *IEEE Geoscience and Remote Sensing Magazine, 9*, 223-270

Brown, C.F., Brumby, S.P., Guzder-Williams, B., Birch, T., Hyde, S.B., Mazzariello, J., Czerwinski, W., Pasquarella, V.J., Haertel, R., Ilyushchenko, S., Schwehr, K., Weisse, M., Stolle, F., Hanson, C., Guinan, O., Moore, R., & Tait, A.M. (2022). Dynamic world, near real-time global 10 m land use land cover mapping. *Scientific Data, 9*, 251

Cao, S., Feng, J., Hu, Z., Li, Q., & Wu, G. (2022). Improving estimation of urban land cover fractions with rigorous spatial endmember modeling. *ISPRS Journal of Photogrammetry and Remote Sensing, 189*, 36-49

Chen, Y., Ge, Y., & Jia, Y. (2017). Integrating object boundary in super-resolution land-cover mapping. *IEEE Journal of Selected Topics in Applied Earth Observations and Remote Sensing, 10*, 219-230

Chen, Y., Zhang, G., Cui, H., Li, X., Hou, S., Ma, J., Li, Z., Li, H., & Wang, H. (2023). A novel weakly supervised semantic segmentation framework to improve the resolution of land cover product. *ISPRS Journal of Photogrammetry and Remote Sensing, 196*, 73-92

Clément, F., Ruiz, J., Rodríguez, M.A., Blais, D., & Campeau, S. (2017). Landscape diversity and forest edge density regulate stream water quality in agricultural catchments. *Ecological Indicators, 72*, 627-639

Deng, C., & Wu, C. (2013). A spatially adaptive spectral mixture analysis for mapping subpixel urban impervious surface distribution. *Remote Sensing of Environment, 133*, 62-70

Dong, Q., Chen, X., Chen, J., Yin, D., Zhang, C., Xu, F., Rao, Y., Shen, M., Chen, Y., & Stein, A. (2022). Bias of area counted from sub-pixel map: Origin and correction. *Science of Remote Sensing, 6*, 100069

Fisher, P. (1997). The pixel: A snare and a delusion. *International Journal of Remote Sensing, 18*, 679-685

Fisher, P.F., & Pathirana, S. (1993). The ordering of multitemporal fuzzy land‐cover information derived from landsat mss data. *Geocarto International, 8*, 5-14

Hao, M., Chen, S., Lin, H., Zhang, H., & Zheng, N. (2024). A prior knowledge guided deep learning method for building extraction from high-resolution remote sensing images. *Urban Informatics, 3*, 6

Hao, M., Dou, G., Zhang, X., Lin, H., & Huo, W. (2023). A subpixel mapping method for urban land use by reducing shadow effects. *IEEE Journal of Selected Topics in Applied Earth Observations and Remote Sensing, 16*, 2163-2177

He, D., Shi, Q., Liu, X., Zhong, Y., & Zhang, L. (2022). Generating 2m fine-scale urban tree cover product over 34 metropolises in china based on deep context-aware sub-pixel mapping network. *International Journal of Applied Earth Observation and Geoinformation, 106*, 102667

He, D., Zhong, Y., Wang, X., & Zhang, L. (2021). Deep convolutional neural network framework for subpixel mapping. *IEEE Transactions on Geoscience and Remote Sensing, 59*, 9518-9539

Holmberg, M., Junttila, V., Schulz, T., Grönroos, J., Paunu, V.-V., Savolahti, M., Minunno, F., Ojanen, P., Akujärvi, A., Karvosenoja, N., Kortelainen, P., Mäkelä, A., Peltoniemi, M., Petäjä, J., Vanhala, P., & Forsius, M. (2023). Role of land cover in finland's greenhouse gas emissions. *Ambio, 52*, 1697-1715

Hong, D., Zhang, B., Li, X., Li, Y., Li, C., Yao, J., Yokoya, N., Li, H., Ghamisi, P., Jia, X., Plaza, A., Gamba, P., Benediktsson, J.A., & Chanussot, J. (2024). Spectralgpt: Spectral remote sensing foundation model. *IEEE Transactions on Pattern Analysis and Machine Intelligence, 46*, 5227-5244

Houghton, R.A., House, J.I., Pongratz, J., van der Werf, G.R., DeFries, R.S., Hansen, M.C., Le Quéré, C., & Ramankutty, N. (2012). Carbon emissions from land use and land-cover change. *Biogeosciences, 9*, 5125-5142

Kasetkasem, T., Arora, M.K., & Varshney, P.K. (2005). Super-resolution land cover mapping using a markov random field based approach. *Remote Sensing of Environment, 96*, 302-314

Keshava, N. (2003). A survey of spectral unmixing algorithms. *lincoln laboratory journal, 14*, 55-78

Kotaridis, I., & Lazaridou, M. (2021). Remote sensing image segmentation advances: A meta-analysis. *ISPRS Journal of Photogrammetry and Remote Sensing, 173*, 309-322

Li, X., Jia, X., Wang, L., & Zhao, K. (2015). On spectral unmixing resolution using extended support vector machines. *IEEE Transactions on Geoscience and Remote Sensing, 53*, 4985-4996

Li, X., Ling, F., Cai, X., Ge, Y., Li, X., Yin, Z., Shang, C., Jia, X., & Du, Y. (2021). Mapping water bodies under cloud cover using remotely sensed optical images and a spatiotemporal dependence model. *International Journal of Applied Earth Observation and Geoinformation, 103*, 102470

Ling, F., Fang, S., Li, W., Li, X., Xiao, F., Zhang, Y., & Du, Y. (2014). Post-processing of interpolation-based super-resolution mapping with morphological filtering and fraction refilling. *International Journal of Remote Sensing, 35*, 5251-5262

Ling, F., Li, X., Xiao, F., Fang, S., & Du, Y. (2012). Object-based sub-pixel mapping of buildings incorporating the prior shape information from remotely sensed imagery. *International Journal of Applied Earth Observation and Geoinformation, 18*, 283-292

Ling, F., Xiao, F., Y., D.U., Xue, H.P., & Ren, X.Y. (2008). Waterline mapping at the subpixel scale from remote sensing imagery with high‐resolution digital elevation models. *International Journal of Remote Sensing, 29*, p.1809-1815

Nguyen, M.Q., Atkinson, P.M., & Lewis, H.G. (2006). Superresolution mapping using a hopfield neural network with fused images. *IEEE Transactions on Geoscience and Remote Sensing, 44*, 736-749

Nguyen, Q.M., Atkinson, P.M., & Lewis, H.G. (2011). Super-resolution mapping using hopfield neural network with panchromatic imagery. *International Journal of Remote Sensing, 32*, 6149-6176

Olthof, I., & Fraser, R.H. (2024). Mapping surface water dynamics (1985–2021) in the hudson bay lowlands, canada using sub-pixel landsat analysis. *Remote Sensing of Environment, 300*, 113895

Otsu, N. (1979). A threshold selection method from gray-level histograms. *IEEE transactions on systems, man, and cybernetics, 9*, 62-66

Pfoch, K.A., Pflugmacher, D., Okujeni, A., & Hostert, P. (2023). Mapping forest fire severity using bi-temporal unmixing of sentinel-2 data - towards a quantitative understanding of fire impacts. *Science of Remote Sensing, 8*, 100097

Pielke Sr, R.A., Pitman, A., Niyogi, D., Mahmood, R., McAlpine, C., Hossain, F., Goldewijk, K.K., Nair, U., Betts, R., Fall, S., Reichstein, M., Kabat, P., & de Noblet, N. (2011). Land use/land cover changes and climate: Modeling analysis and observational evidence. *WIREs Climate Change, 2*, 828-850

Plaza, A., Martín, G., Plaza, J., Zortea, M., & Sánchez, S. (2011). Recent developments in endmember extraction and spectral unmixing. *Optical Remote Sensing: Advances in Signal Processing and Exploitation Techniques*, 235-267

Plaza, A., Martinez, P., Perez, R., & Plaza, J. (2002). Spatial/spectral endmember extraction by multidimensional morphological operations. *IEEE Transactions on Geoscience and Remote Sensing, 40*, 2025-2041

Shang, C., Li, X., Foody, G.M., Du, Y., & Ling, F. (2020). Superresolution land cover mapping using a generative adversarial network. *IEEE Geoscience and Remote Sensing Letters*, 1-5

Shaw, R., & Banba, M. (2017). Land use management in disaster risk reduction: An overview. *Land use management in disaster risk reduction: Practice and cases from a global perspective*, 3-12

Shi, C., & Wang, L. (2014). Incorporating spatial information in spectral unmixing: A review. *Remote Sensing of Environment, 149*, 70-87

Shi, W., Goodchild, M., Batty, M., Li, Q., Liu, X., & Zhang, A. (2022). Prospective for urban informatics. *Urban Informatics, 1*, 2

Tatem, A.J., Lewis, H.G., Atkinson, P.M., & Nixon, M.S. (2002). Super-resolution land cover pattern prediction using a hopfield neural network. *Remote Sensing of Environment, 79*, 1-14

Tolpekin, V.A., & Hamm, N.A.S. (2008). Fuzzy super resolution mapping based on markov random fields. In, *IGARSS 2008 - 2008 IEEE International Geoscience and Remote Sensing Symposium* (pp. II-875-II-878)

Wang, C., Wang, Y., Wang, R., & Zheng, P. (2018). Modeling and evaluating land-use/land-cover change for urban planning and sustainability: A case study of dongying city, china. *Journal of Cleaner Production, 172*, 1529-1534

Wang, L., Shi, C., Diao, C., Ji, W., & Yin, D. (2016). A survey of methods incorporating spatial information in image classification and spectral unmixing. *International Journal of Remote Sensing, 37*, 3870-3910

Wang, P., Huang, M., Wang, L., Zhang, G., Leung, H., & Zhao, C. (2022). Spatiotemporal subpixel mapping based on priori remote sensing image with variation differences. *IEEE Journal of Selected Topics in Applied Earth Observations and Remote Sensing, 15*, 7556-7575

Wang, Q., Shi, W., & Atkinson, P.M. (2014a). Sub-pixel mapping of remote sensing images based on radial basis function interpolation. *ISPRS Journal of Photogrammetry and Remote Sensing, 92*, 1-15

Wang, Q., Shi, W., & Wang, L. (2014b). Allocating classes for soft-then-hard subpixel mapping algorithms in units of class. *IEEE Transactions on Geoscience and Remote Sensing, 52*, 2940-2959

Wang, Q., Zhang, C., Tong, X., & Atkinson, P.M. (2020). General solution to reduce the point spread function effect in subpixel mapping. *Remote Sensing of Environment, 251*, 112054

Xu, F., Heremans, S., & Somers, B. (2022). Urban land cover mapping with sentinel-2: A spectro-spatio-temporal analysis. *Urban Informatics, 1*, 8

Yin, Z., Wu, Y., Wu, P., Hao, Z., & Ling, F. (2023). Super-resolution mapping with a fraction error eliminating cnn model. *IEEE Transactions on Geoscience and Remote Sensing, 61*, 1-18

Zare, A., Gader, P., Bchir, O., & Frigui, H. (2013). Piecewise convex multiple-model endmember detection and spectral unmixing. *IEEE Transactions on Geoscience and Remote Sensing, 51*, 2853-2862

Zhang, C., Wang, Q., Lu, P., Ge, Y., & Atkinson, P.M. (2022). Fast and slow changes constrained spatio-temporal subpixel mapping. *IEEE Transactions on Geoscience and Remote Sensing, 60*, 1-16

Zhang, X., Ge, Y., Chen, J., Ling, F., Wang, Q., Du, D., & Xiang, R. (2023). High-quality super-resolution mapping using spatial deep learning. *iScience, 26*, 106875

Zhang, X., Liu, L., Chen, X., Gao, Y., Xie, S., & Mi, J. (2021). Glc_fcs30: Global land-cover product with fine classification system at 30 m using time-series landsat imagery. *Earth System Science Data, 13*, 2753-2776

Zhao, J., Zhong, Y., Hu, X., Wei, L., & Zhang, L. (2020). A robust spectral-spatial approach to identifying heterogeneous crops using remote sensing imagery with high spectral and spatial resolutions. *Remote Sensing of Environment, 239*, 111605